Supplementary information
for

High oxide ion and proton conductivity in a disordered hexagonal perovskite

S. Fop†*, K. S. McCombie†, E. J. Wildman†, J. M. S. Skakle†, J. T. S. Irvine‡, P. A. Connor‡, C. Savaniu‡, C. Ritter§ and A. C. Mclaughlin†*

† Department of Chemistry, University of Aberdeen, Meston Walk, Aberdeen AB24 3UE, United Kingdom.

‡ School of Chemistry, University of St Andrews, St Andrews, Fife KY16 9ST, UK.

§ Institut Laue Langevin, 71 Avenue des Martyrs, BP 156, F-38042 Grenoble Cedex 9, France.

* Authors to whom correspondence should be addressed

A.C.M. (email: a.c.mclaughlin@abdn.ac.uk) or S.F. (email: sacha.fop1@abdn.ac.uk).

S1. Synthesis and sample characterisation

S1.1 Synthesis and laboratory X-ray diffraction

$Ba_7Nb_4MoO_{20}$ samples were prepared by solid-state reaction of stoichiometric amounts of $BaCO_3$ (99.999%, Aldrich), MoO_3 (99.5+%, Aldrich) and Nb_2O_5 (99.99%, Aldrich). The starting materials were ground, pressed into a pellet, heated at 1050 °C for 48 hours and then cooled to room temperature at 5 °C/min. The heating step was repeated until a phase pure product was obtained. Garcia-González *et al* reported the synthesis of $Ba_7Nb_4MoO_{20}$ at 1300 °C [1]. However, attempts to obtain a phase pure product at 1300 °C were unsuccessful, due to the formation of impurities of $Ba_3NbMoO_{8.5}$ and $Ba_5Nb_4O_{15}$. These impurities are observed to form above 1100 °C.

Room temperature X-ray powder diffraction (XRD) patterns were collected on a PANalytical Empyrean diffractometer equipped with a Cu Kα tube and a Johansson monochromator. Data were recorded in the range 10° < 2θ < 100°, with a step size of 0.013°. The XRD pattern of the as prepared material confirms the sample to be phase pure (Figure S1). The X-ray diffraction pattern could be indexed with the space group $P\bar{3}m1$ (a = 5.8701 (1) Å, c = 16.5378 (3) Å), in agreement with Garcia-González *et al* [1].

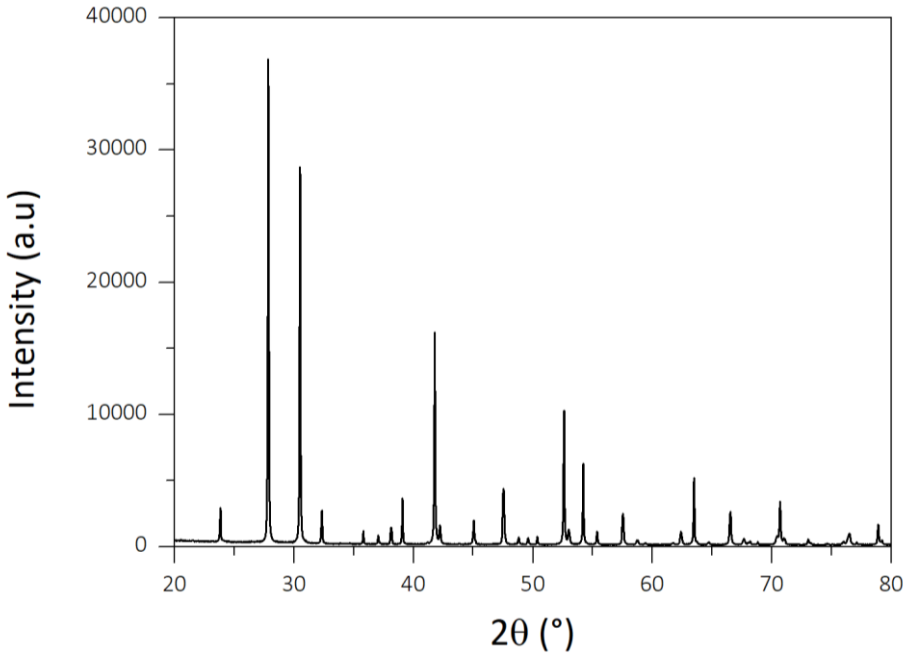

Figure S1. XRD pattern of as prepared $Ba_7Nb_4MoO_{20}$

S1.2 SEM-EDS analysis

SEM-EDS analysis was performed using a field emission gun Carl Zeiss Gemini SEM 300 equipped with an AZtec Energy EDS analysis system with an XMax 80 detector and an AZtecHKL EBSD analysis system with a Nordlys Nano EBSD camera (Oxford Instruments Ltd.). SEM micrographs were collected on the surface and section of a carbon-coated dense (~ 94% of the theoretical neutron diffraction density) $Ba_7Nb_4MoO_{20}$ pellet. Secondary electron (SE) images show grains ranging in size between ~ 1 – 5 µm; no secondary phases were observed in the backscattering (BSE) images of the surface and section of the pellet (Figure S2).

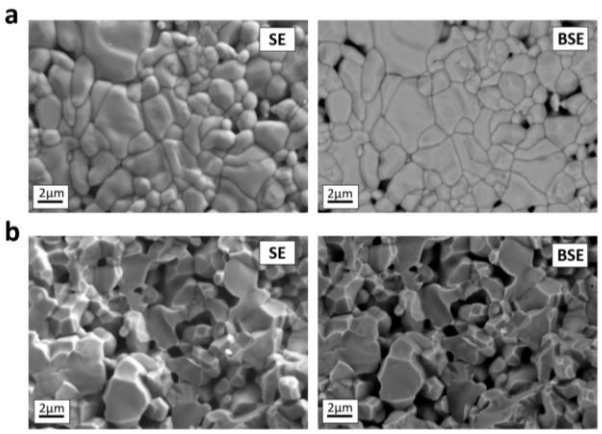

Figure S2. SEM micrographs of the surface (**a**) and section (**b**) of a dense $Ba_7Nb_4MoO_{20}$ pellet.

Energy dispersive spectroscopy (EDS) analysis was performed on two different carbon-coated powder samples; an as-prepared sample (Ba7) and a powder heated at 1200 °C 5h + 1050 °C 48h (Ba7-1200), which is the sintering/annealing procedure employed to obtain dense pellet samples (see Supplementary Information S4). For each sample, data were collected on 20 randomly selected crystallites in two different sites. A typical EDS scan is shown in Figure S3 for sample Ba7.

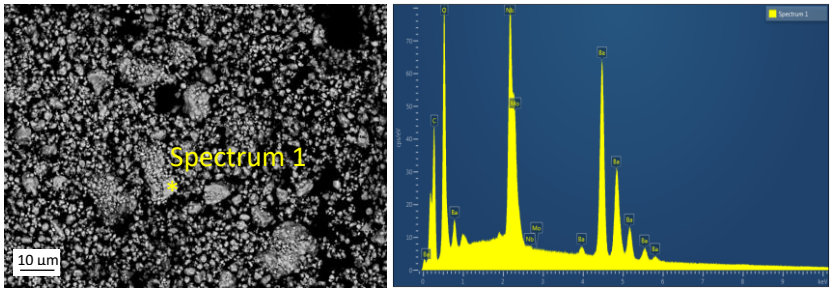

Figure S3. Typical EDS scan for sample Ba7.

The EDS analysis evidences that the $Ba_7Nb_4MoO_{20}$ powders have homogeneous composition. The results for the Ba, Nb and Mo cations are reported in Table S1. For stoichiometric $Ba_7Nb_4MoO_{20}$ the theoretical atomic percentages are: Ba, 21.875%; Nb, 12.500%; Mo, 3.125%. The average atomic percentages calculated from the measurements on Ba7 and Ba7-1200 are close to the theoretical values within instrument resolution and standard deviations. The atomic percentages obtained from the EDS scan of three randomly selected areas of the dense $Ba_7Nb_4MoO_{20}$ pellet (Ba7 pellet) show similar agreement.

Table S1. Results from EDS analysis on powder and pellet $Ba_7Nb_4MoO_{20}$ samples.

	Ba %	**Nb %**	**Mo %**
Theoretical	21.875	12.500	3.125
Ba7	21.84 (±0.31)	12.35 (±0.41)	3.06 (±0.40)
Ba7-1200	21.91 (±0.33)	12.52 (±0.40)	3.11 (±0.35)
Ba7 pellet	21.89 (±0.42)	12.49 (±0.37)	3.13 (±0.32)

The ratio between the atomic percentages gives average composition of $Ba_{7.13}Nb_{4.03}Mo$ for Ba7, $Ba_{7.04}Nb_{4.02}Mo$ for Ba7-1200 and $Ba_{6.99}Nb_{3.99}Mo$ for the dense pellet sample. All the samples exhibit a cationic ratio in agreement, within the expected errors, with the nominal Ba_7Nb_4Mo cationic composition.

S2. Phase diagram

Figure S4 presents the compositional pseudo-ternary phase diagram of the Ba-Nb-Mo-O system; the green cross corresponds to $Ba_7Nb_4MoO_{20}$.

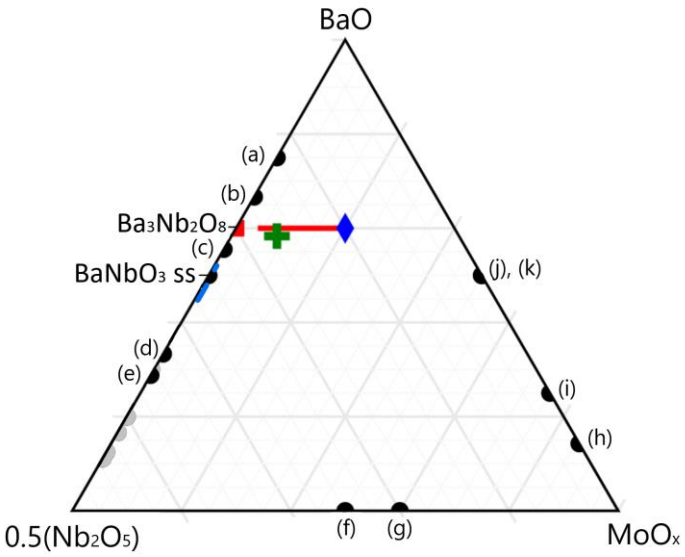

Figure S4: Compositional pseudo-ternary phase diagram of the Ba-Nb-Mo-O system, normalised to one cation at each vertex. Phases which have a reported crystal structure are shown. The black circles are reported phases, including the short solid solution of $BaNbO_3$ (perovskite, blue line) (ref. 2). The red square is $Ba_3Nb_2O_8$ (ref. 3) and the blue diamond is $Ba_3NbMoO_{8.5}$ (ref. 4), with the red solid solution region $Ba_3Mo_{1-x}Nb_{1+x}O_{8.5-\delta}$ (ref. 5). The green cross is $Ba_7Nb_4MoO_{20}$ (compositionally close but structurally distinct from the solid solution) (ref. 1).

Phases: (a) $Ba_6Nb_2O_{11}$ (ref. 6); (b) $Ba_4Nb_2O_9$ (ref. 7); (c) $Ba_5Nb_4O_{15+d}$ (ref. 8); (d) $BaNb_2O_6$ (ref. 9); (e) $Ba_3Nb_{10}O_{28}$ and $Ba_{3.3}Nb_{10}O_{28.3}$ (ref. 10); (f) $NbMoO_4$ (ref. 11); (g) $Mo_3Nb_2O_{14}$ (ref. 12); (h) $BaMo_6O_{10}$ (ref. 13); (i) $BaMo_3O_{10}$ (ref. 14); (j) $BaMoO_4$ (Scheelite) (ref. 15); (k) $BaMoO_3$ (perovskite) (ref. 16). The phases in the Nb-rich region (>75%, light grey) are reduced niobates: $BaNb_4O_6$ and $BaNb_5O_8$ (ref. 17), $BaNb_7O_9$ (ref. 18), $BaNb_8O_{14}$ (ref. 19), $Ba_3Nb_5O_{15}$ (ref. 20), $Ba_2Nb_5O_9$ (ref. 21). The data are taken from the Inorganic Crystal Structure Database and the figure drawn using ternaryplot.com.

S3. Phase stability tests

Phase stability tests were conducted by annealing powder samples of $Ba_7Nb_4MoO_{20}$ under 5% H_2 (in N_2) and pure CO_2 (1 atm) for 24 h at various temperatures. The samples phase purity was checked by collecting X-ray powder diffraction patterns post-annealing. XRD patterns of

the samples treated under 5% H_2 (in N_2) were collected on a PANalytical X'Pert powder diffractometer equipped with a Cu Kα tube, in the range 20° < 2θ < 60°, with a step size of 0.013°. Samples treated in pure CO_2 were examined using a PANalytical Empyrean diffractometer equipped with a Cu Kα tube and a Johansson monochromator, with data recorded in the range 20° < 2θ < 60° and using a step size of 0.013°.

Figure S5a shows the XRD patterns collected on the sample after annealing under 5% H_2 (in N_2). The XRD data show that post-annealing there is no change in crystal structure, with no evidence of secondary phases, indicating that the $Ba_7Nb_4MoO_{20}$ phase is stable in the reducing 5% H_2 (in N_2) environment. For comparison, other leading oxide ion conductors such as the Bi and Ce oxides and $Ba_2In_2O_5$ degrade or present impurity phases at low oxygen partial pressures [22, 23]. The Mo-containing oxide ion conductor $La_2Mo_2O_9$ is unstable under reducing conditions [24], dramatically degrading to $La_7Mo_7O_{30}$, $La_{2.4}Mo_{1.6}O_8$ and an amorphous phase with composition $La_2Mo_2O_{6.88}$ above 700 °C [25, 26, 27].

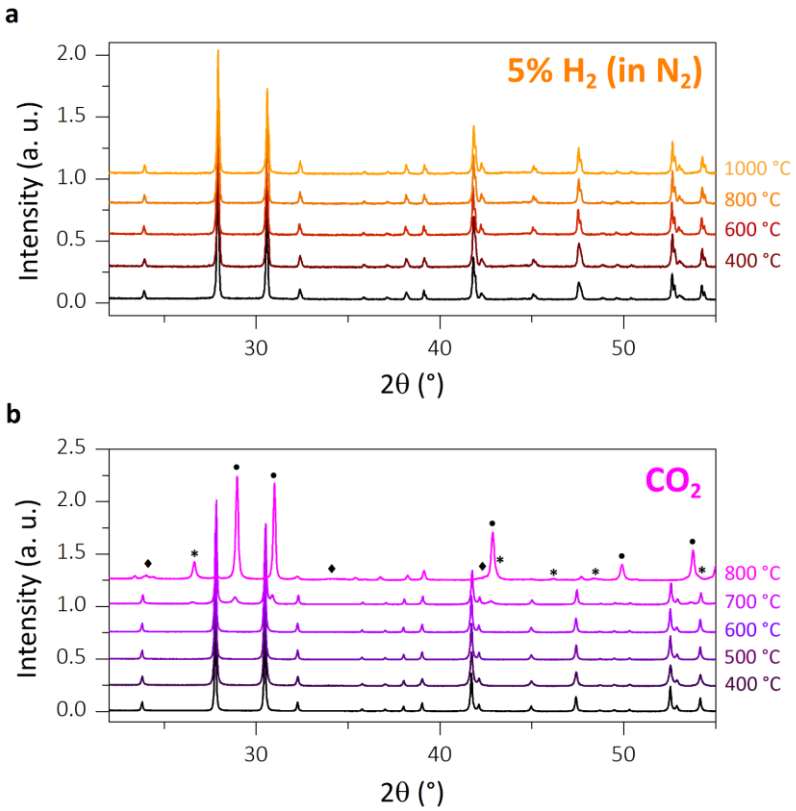

Figure S5. XRD pattern of $Ba_7Nb_4MoO_{20}$ after annealing for 24 h at various temperatures under 5% H_2 (in N_2) (**a**) and pure CO_2 (**b**). Symbols in **b** indicate reflections of $BaCO_3$ (♦), $BaMoO_4$ (∗) and $Ba_5Nb_4O_{15}$ (●).

To further prove the stability of $Ba_7Nb_4MoO_{20}$ against reduction, thermogravimetric analysis was performed with a Mettler Toledo TGA 2 coupled with a Hiden Quadrupole Mass Spectrometer in dry air and 5% H_2 (in N_2) atmospheres on a previously dried $Ba_7Nb_4MoO_{20}$ powder sample. The TGA in Figure S6 shows a weight loss above 200 °C in both atmospheres. The weight loss is attributed to release of water, as evidenced from the corresponding mass spectrometry peaks at 18 amu. No loss of molecular oxygen is detected in the mass spectrum collected at 32 amu, thus evidencing no change in the oxygen stoichiometry upon heating in air and 5% H_2.

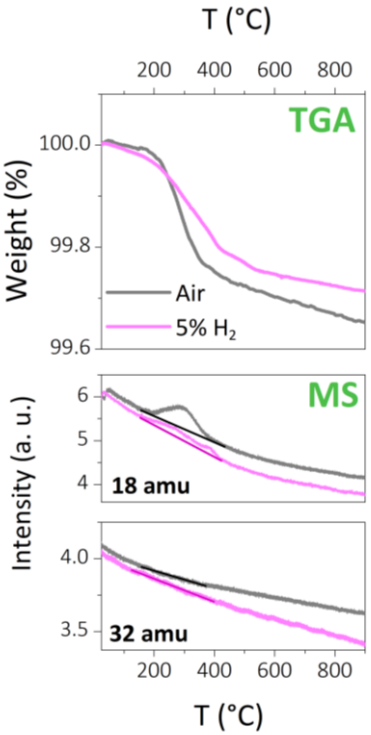

Figure S6. Results of the TGA-MS analysis on a pre-dried $Ba_7Nb_4MoO_{20}$ sample under dry air and 5% H_2 (in N_2) atmospheres. Top panel shows the thermogravimetric (TGA) diagram, while the bottom ones are the mass spectroscopy diagrams obtained at 18 amu (H_2O) and 32 amu (O_2).

For practical utilisation in SOFCs and PCFCs, in addition to stability under reducing conditions, good chemical stability against CO_2 is highly desirable, since the use of hydrocarbon fuels (such as methane) can lead to the production of CO_2. Carbon dioxide is an acidic gas and can react with alkaline earth-containing oxides, leading to the production of carbonates and other secondary phases. Chemical instability in CO_2-containing atmospheres is a severe problem for

proton conducting $BaCeO_3$-based oxides [28, 29]. For example, $BaCe_{0.9}Y_{0.1}O_{2.95}$ easily decomposes to $BaCO_3$ and CeO_2 in pure CO_2 below 1150 °C, and in 9% CO_2 (in Ar) below 750 °C [30]. Doped $BaCeO_3$ phases show signs of ageing and degradation due to reaction with atmospheric CO_2 even at ambient conditions [31]. Acceptor-doped $BaZrO_3$ materials possess greater chemical stability than the cerates [28]. However, recent studies on $BaZr_{1-x}Y_xO_{3-\delta}$ compounds have evidenced formation of $BaCO_3$ and deterioration of the mechanical properties after annealing in pure CO_2 for 10 – 20 h in the temperature range 550 – 750 °C [32].

The stability of $Ba_7Nb_4MoO_{20}$ against carbon dioxide was checked by annealing a powder sample under pure CO_2. XRD patterns collected on the sample post-annealing evidence that the phase is stable up to 600 °C under 1 atm of CO_2 (Figure S5b). The XRD pattern collected after annealing at 700 °C shows the main $Ba_7Nb_4MoO_{20}$ phase with the presence of additional $BaMoO_4$ and $Ba_5Nb_4O_{15}$ phases. After heating at 800 °C, $Ba_7Nb_4MoO_{20}$ is almost completely degraded to $BaMoO_4$, $Ba_5Nb_4O_{15}$ and $BaCO_3$. These results show that $Ba_7Nb_4MoO_{20}$ is stable under pure CO_2 in the temperature range 400 – 600 °C, useful for potential applications in intermediate temperature SOFCs and PCFCs.

For potential use as an electrolyte material, $Ba_7Nb_4MoO_{20}$ should be chemically compatible with typical electrode materials. Nickel oxide is commonly employed to form NiO/YSZ cermet anodes for solid oxide fuel cells [33]. Cobaltite $Ba_{0.5}Sr_{0.5}Co_{0.8}Fe_{0.2}O_{3-\delta}$ (BSCF) is a cathode material with excellent electrochemical activity at low temperatures and is utilised in both SOFC and PCFC systems [34, 35].

Preliminary compatibility tests between $Ba_7Nb_4MoO_{20}$ and NiO and BSCF were conducted by annealing powder mixtures. NiO (Aldrich, 99.999%) and BSCF (prepared from solid state reaction at 1000 °C) were mixed in a 50:50 wt.% ratio with $Ba_7Nb_4MoO_{20}$ and fired at various temperatures for 24 hours. The mixtures were subsequently examined by collecting X-ray powder diffraction patterns post-annealing.

Figure S7a shows no evidence of any reaction between $Ba_7Nb_4MoO_{20}$ and NiO up to 800 °C. At 900 °C, $BaNi_{0.33}Nb_{0.67}O_3$ starts forming with subsequent segregation of $BaMoO_4$ at 1000 °C. Similarly, no reaction occurs between $Ba_7Nb_4MoO_{20}$ and BSCF up to 800 °C; various secondary phases ($Ba_{0.5}Sr_{0.5}MoO_4$, $Ba_3SrNb_2O_9$, $Ba_3CoNb_2O_9$ and an unidentified phase) however form at 1000 °C (Figure S7b). Cobaltite BSCF materials have been reported to react with several electrolyte compounds. W-doped $La_2Mo_2O_9$, shows a dramatic reaction with BSCF above

500 °C, with the LAMOX phase almost disappearing at 700 °C [36]. BSCF reacts with the co-doped proton conductor $Ba_{0.98}Ce_{0.6}Zr_{0.2}Y_{0.2}O_{3-\delta}$ at 900 °C [37], and with $La_{0.995}Ca_{0.005}NbO_4$ at 1150 °C [38].

Overall, $Ba_7Nb_4MoO_{20}$ presents good compatibility with NiO and BSCF, without formation of any secondary phases up to 800 °C, indicating that $Ba_7Nb_4MoO_{20}$ can be employed with NiO/BSCF electrode materials in an intermediate temperature range 300 – 700 °C. The reactivity of $Ba_7Nb_4MoO_{20}$ and NiO/BSCF above 900 °C suggests that high temperature (> 1000 °C) annealing to fix the electrolyte and electrodes should be avoided. Methods allowing lower fixing temperatures such as spray deposition, spray pyrolysis etc. or the use of electrode nanoparticles should be preferred**.** Alternative electrode materials (free of Sr and Ni for example) may also exhibit greater compatibility.

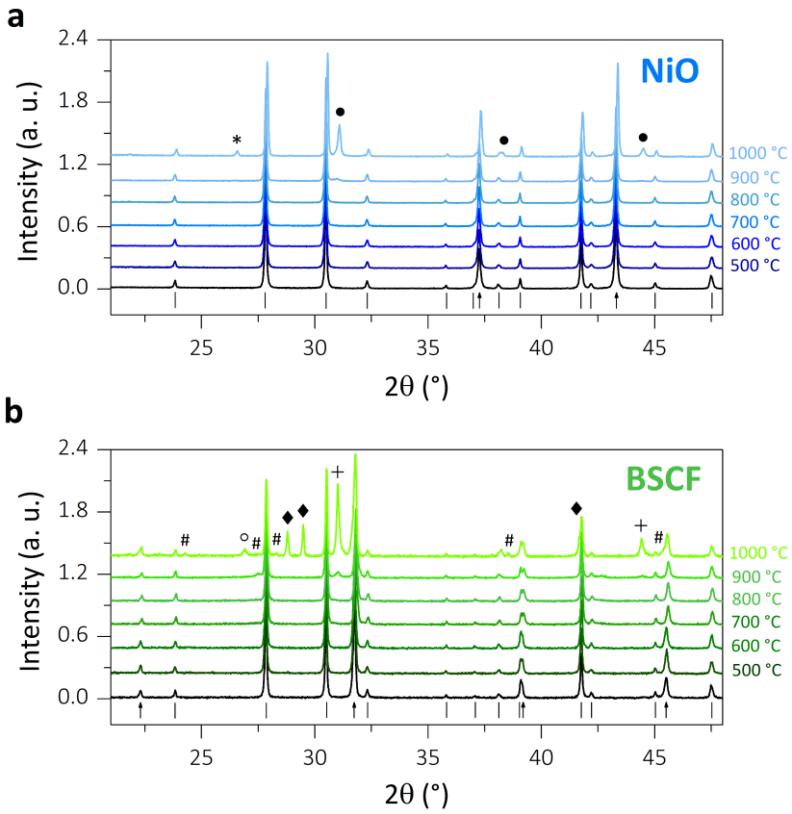

Figure S7. XRD patterns of $Ba_7Nb_4MoO_{20}$/NiO (**a**) and $Ba_7Nb_4MoO_{20}$/BSCF (**b**) at room temperature (black line) and after annealing at various temperatures. Vertical tics indicate reflections of $Ba_7Nb_4MoO_{20}$, while the arrows indicate reflections of NiO and BSCF. Symbols in **a** indicate reflections of $BaMoO_4$ (∗) and $BaNi_{0.33}Nb_{0.67}O_3$ (●); symbols in **b** indicate $Ba_{0.5}Sr_{0.5}MoO_4$ (○), $Ba_3SrNb_2O_9$ (♦), $Ba_3CoNb_2O_9$ (+) and an unidentified phase (#).

S4. Preparation of dense samples

Dense pellet samples for AC impedance spectroscopy measurements and concentration cell experiments were prepared from powder samples of $Ba_7Nb_4MoO_{20}$. In order to achieve ~ 95% of the theoretical neutron diffraction density, pellets of ~ 10 mm diameter and ~ 1 mm thickness were sintered at 1200 °C for 5 h, cooled to 1050 °C at 5 °C/min and subsequently annealed at that temperature for 48 h (1200 °C 5h + 1050 °C 48h).

In order to produce high density materials, a higher temperature sintering step is required. Heating of $Ba_7Nb_4MoO_{20}$ at 1200 °C for 5 h results in the appearance of impurity phases (< 1%) of $Ba_3NbMoO_{8.5}$ and $Ba_5Nb_4O_{15}$ (Figure S8). The $Ba_3NbMoO_{8.5}$ phase forms above 1100 °C [4, 39], and demixing of Mo from $Ba_7Nb_4MoO_{20}$ then results in the development of the Nb-rich compound $Ba_5Nb_4O_{15}$. Subsequent annealing at 1050 °C after the 1200 °C step results in a phase pure material, as confirmed by X-ray diffraction on both the powder and pellet samples.

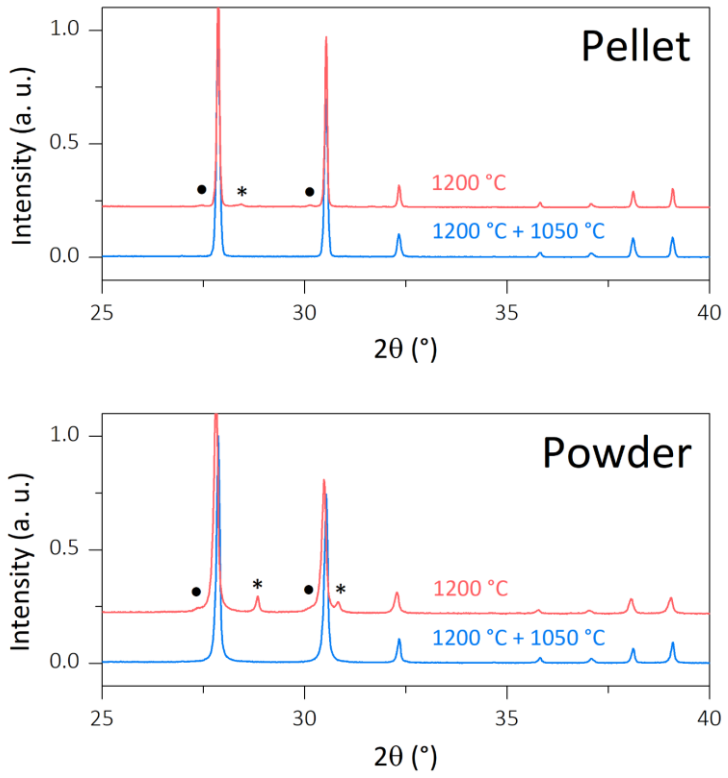

Figure S8. XRD patterns collected on powder and pellet samples of $Ba_7Nb_4MoO_{20}$ after heating at 1200 °C for 5h (red line) and 1200 °C 5 h + 1050 °C 48 h (blue line). Symbols indicate reflections of $Ba_3NbMoO_{8.5}$ (●) and $Ba_5Nb_4O_{15}$ (∗).

S5. Electrical characterisation

S5.1 Impedance spectroscopy under dry and humidified air

Typical impedance spectra recorded on a dense $Ba_7Nb_4MoO_{20}$ pellet under a flow of dry air ($pH_2O < 10^{-4}$ atm) are presented in Figure S9. At the lower temperatures (between 160 °C and 345 °C), typical complex impedance plots show two depressed arcs in the high- and intermediate-frequency regions, together with a well-defined electrode response at lower frequencies (Figure S9a). The small high-frequency arc presents capacitance values of ~ 7 – 10 pF cm^{-1} and can be ascribed to the bulk response of the material, while the broader arc at intermediate frequencies shows capacitance of ~ 0.10 – 0.30 nF cm^{-1}, characteristic of a grain boundary response [40]. The bulk response gradually disappears from the frequency window of the scan and is visible up to 360 °C (Figure S9b). Above this temperature, the grain boundary arc along with a pronounced spike signal inclined at ~ 45° indicative of Warburg diffusion are observed (Figure S9c). At 510 °C, the low frequency Warburg response turns over to form a semicircle with large capacitance values of ~ 5 – 7 x 10^{-5} F cm^{-1} and only part of the grain boundary arc is visible as the temperature rises further (Figure S9d, e). Above 670 °C the electrode response dominates the impedance data (Figure S9f), and inductive effects from the experimental setup appear for T > 715 °C. Total resistivity values ($R_b + R_{gb}$) were extracted from the intercept of the grain boundary semicircular arc at low frequencies in the temperature range 160 – 655 °C. Above 670 °C, the intercept of the electrode signal at high frequency was extracted as the total resistivity.

Impedance spectroscopy measurements were performed also in air + H_2O (humidified air, pH_2O ~ 0.021 atm). Figure S10 shows characteristic impedance plots recorded under a flow of humidified air. The high-frequency bulk arc (capacitance ~ 8 – 9 pF cm^{-1}) is visible only at low temperatures, between 120 °C and 300 °C (Figure S10a). The grain boundary and electrode responses at intermediate and low frequencies are poorly separated (Figure S10b, c). Poor resolution between the grain and the electrode responses is most likely due to the presence of a charge transfer effect (capacitance ~ 0.1 µF cm^{-1}) at the electrode-electrolyte interface. As the temperature rises, the charge transfer resistance gradually decreases, leading to better separation between the grain boundary response and the pronounced Warburg spike signal. A similar behaviour has been reported in doped $BaCeO_3$ [41]. The grain boundary response (capacitance ~ 0.20 – 0.40 nF cm^{-1}) and electrode responses are fully

resolved above 405 °C (Figure S10d). The depressed grain boundary semicircle is only partially visible as the temperature increases, and the electrode spike becomes the most prominent feature in the complex impedance plots, collapsing over to form a semicircle with large capacitance values of 8 – 9 x 10^{-5} F cm^{-1} above 555 °C (Figure S10e). Above 600 °C, the electrode response is the only visible feature, together with an inductance component generated by the leads of the measuring impedance jig (Figure S10f). Total resistivity values in the temperature range 120 – 628 °C were extracted from the estimated low frequency intercept of the grain boundary arc. Above 645 °C, the value of the high frequency intercept of the electrode arc was taken as the total resistivity.

The extracted total resistivity values were employed to obtain the total conductivities of $Ba_7Nb_4MoO_{20}$ in dry air and air + H_2O reported in the Arrhenius plot of Figure 1b and Figure 2c, d in the manuscript.

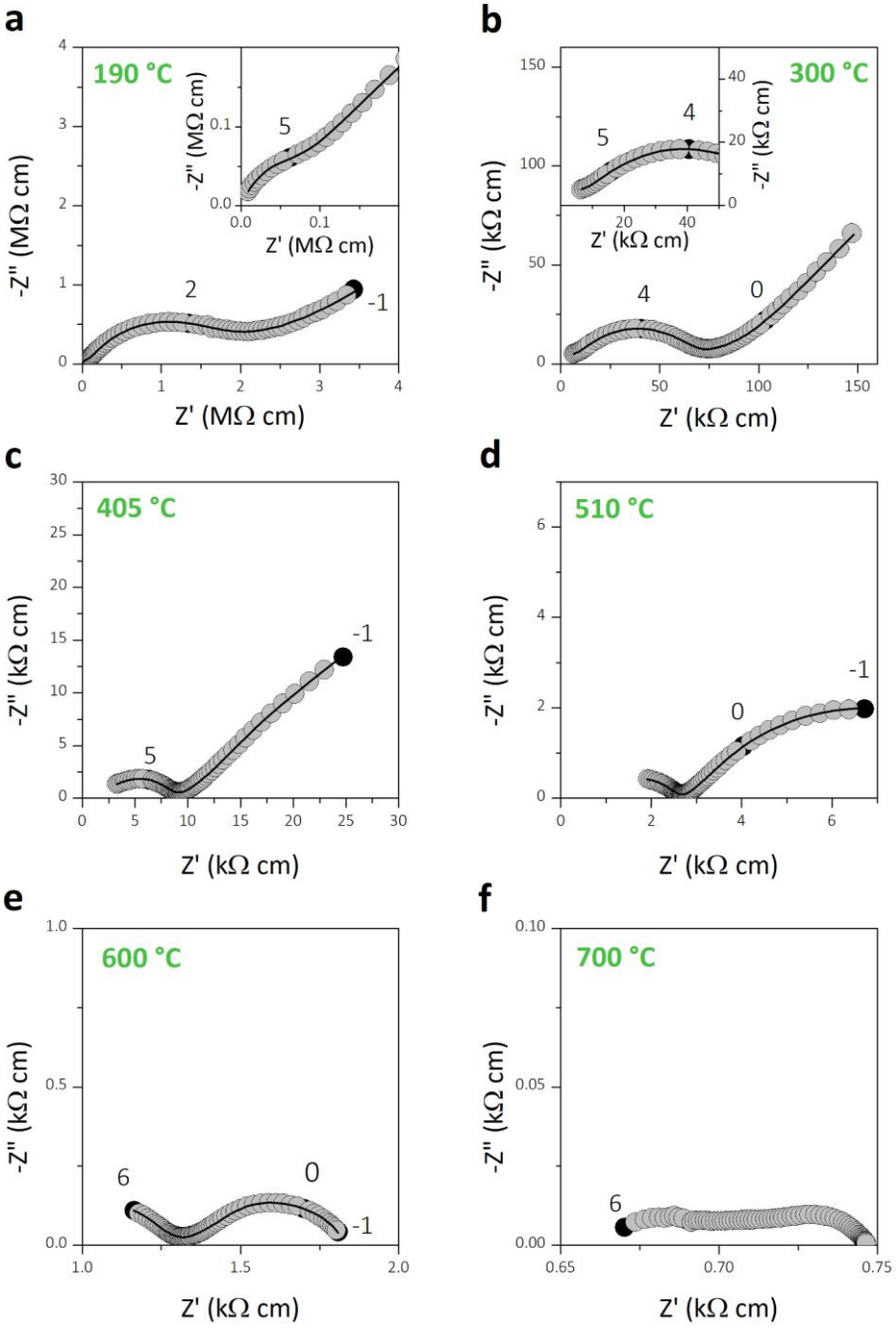

Figure S9. Complex impedance plots recorded in dry air (pH_2O < 10^{-4} atm) at various temperatures. Insets in **a** and **b** show magnification of the high frequency region. The numbers and corresponding filled circles indicate selected frequency decades; the black line is the equivalent circuit fitting.

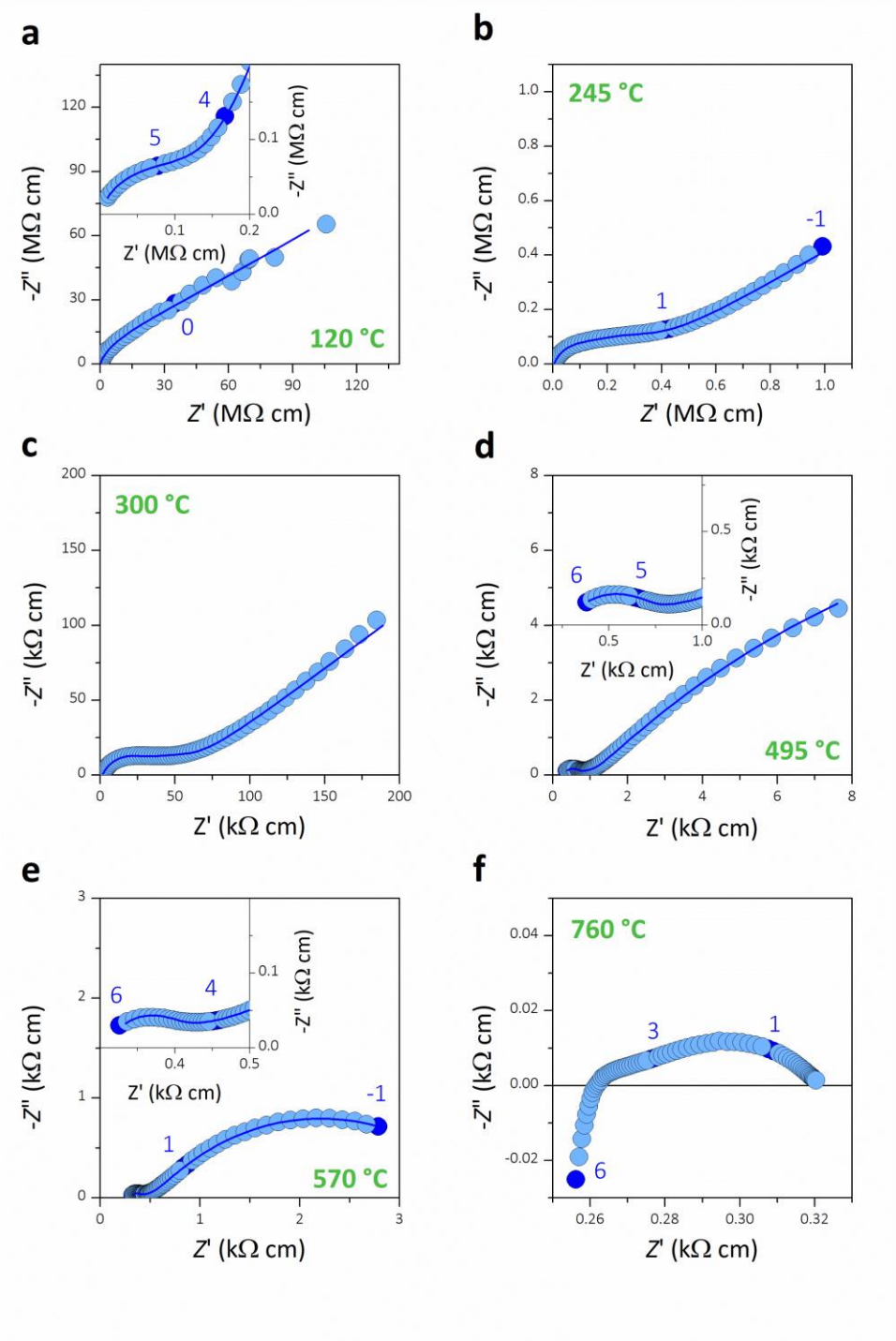

Figure S10. Complex impedance plots recorded in air + H_2O (pH_2O ~ 0.021 atm) at various temperatures. Insets in **a**, **d** and **e** show magnification of the high frequency region. The numbers and corresponding filled circles indicate selected frequency decades; the blue line is the equivalent circuit fitting.

Figure S11 shows a comparison between the complex impedance data collected in dry air and humidified air atmospheres. The electrode response at low frequencies becomes more prominent when switching to humidified air as expected for a proton conductor.

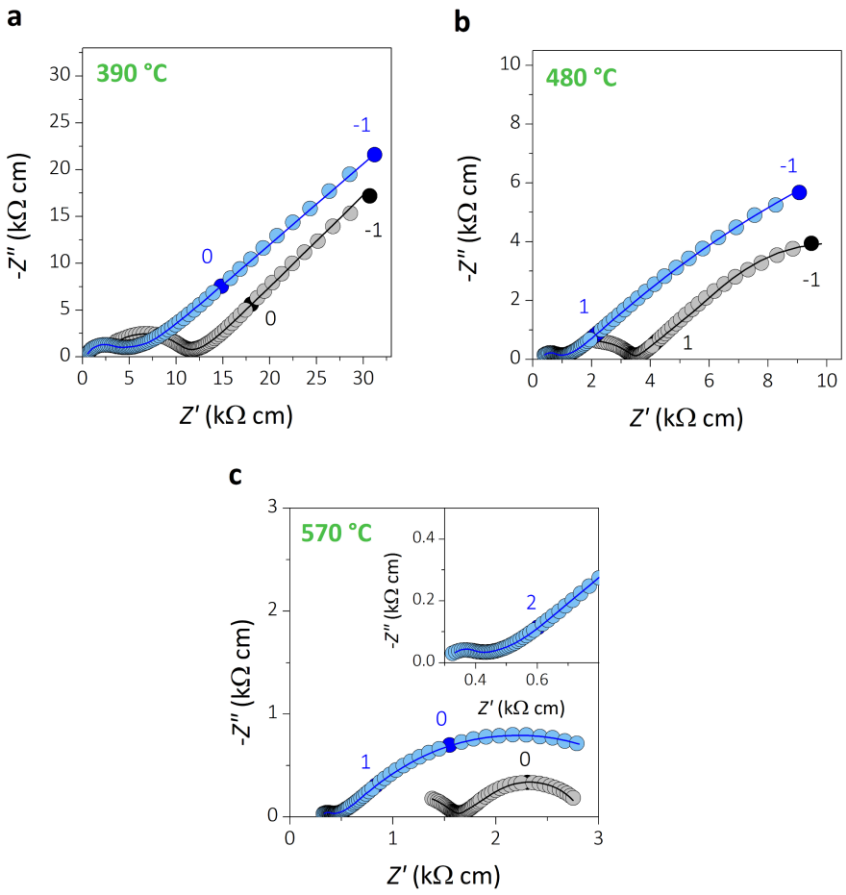

Figure S11. Comparison between the complex impedance plots collected in dry air (grey circles) and humidified air (light blue circles) at various temperatures. The inset in **c** shows magnification of the high frequency region. The numbers and corresponding filled circles indicate selected frequency decades; lines correspond to the equivalent circuit fitting.

S5.2 Conductivity under different gases (O_2, N_2 and 5% H_2)

Typical complex impedance plots obtained from measurements in dry O_2 and N_2 flows are reported in Figure S12, together with plots of the data collected in dry air. The high-frequency bulk arc is independent of the atmosphere (Figure S12a), and so is the grain boundary arc at intermediate frequencies (Figure S12b, inset). The behaviour of the low-frequency electrode signal is consistent with oxygen ion conduction and Warburg diffusion (Figure S12b). The

Arrhenius plot in Figure S12c, d confirms that the total conductivity does not depend on the oxygen partial pressure at high pO_2 values.

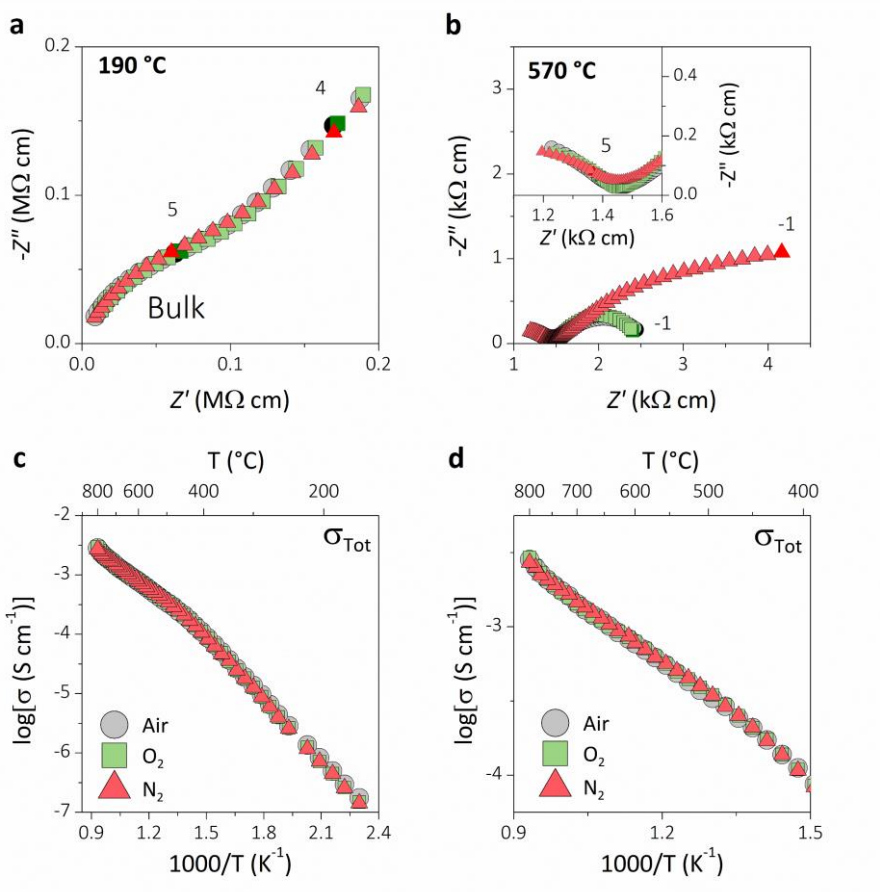

Figure S12. a, **b** Complex impedance plots recorded at 190 °C and 570 °C in dry O_2 (green squares) and dry N_2 (red triangles); data obtained in dry air (grey circles) are reported for comparison. The inset in **b** shows a magnification of the high frequency region. The numbers and corresponding filled symbols indicate selected frequency decades. **c**, **d** Arrhenius plot of the total conductivity under dry air, O_2 and N_2 flows; **b** shows a magnification of the total conductivity data at higher temperatures.

Complex impedance plots recorded in dry and humidified 5% H_2 (in N_2) are presented in Figure S13. Figure S13a, which makes a comparison with the data collected in air + H_2O, evidences how the more reducing conditions in 5% H_2 (in N_2) does not have a significant effect on the bulk signal at high frequencies at 134 °C. The complex impedance plots show clear Warburg/electrode responses at all temperatures (Figure S13b, c), providing further evidence of prevalent ionic conductivity [42]. The Arrhenius plot in Figure S13d shows that the total conductivity in dry and humidified 5% H_2 (in N_2) is substantially higher than conductivity in

dry air above ~ 300 °C. The total conductivity in 5% H_2 is comparable with the total conductivity in air + H_2O, showing a non-linear behaviour at high temperatures typical of proton conduction and a similar increase at the structural rearrangement.

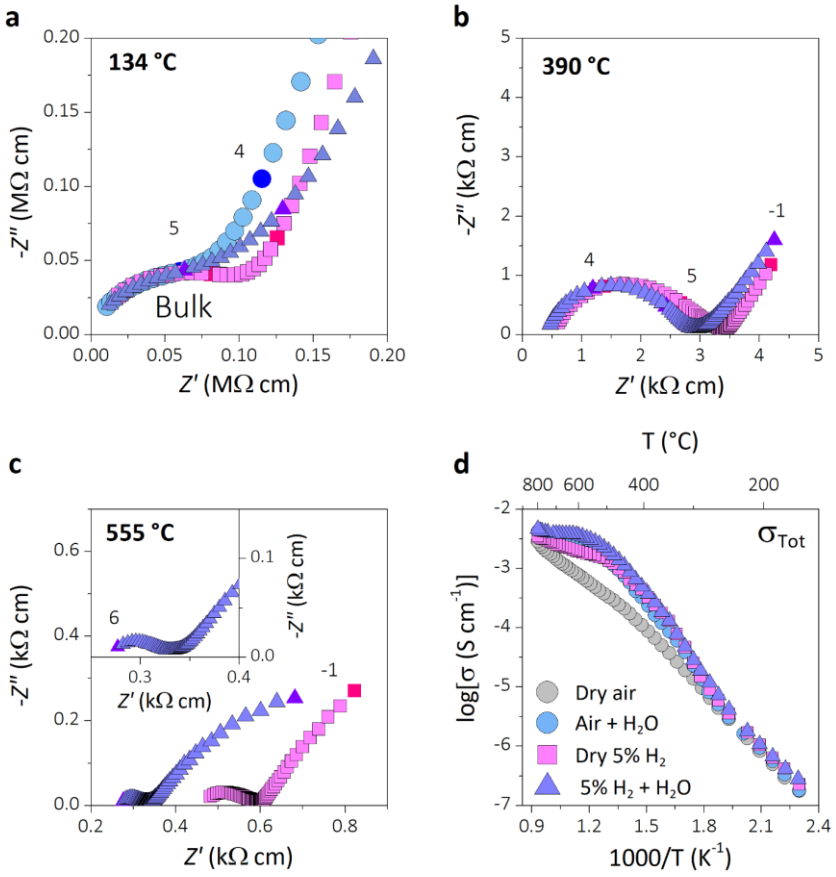

Figure S13. a, **b**, **c** Complex impedance plots recorded at 134 °C, 390 °C and 555 °C in dry 5% H_2 (in N_2) (magenta squares) and humidified 5% H_2 (in N_2) (purple triangles). Data obtained in wet air (pale blue circles) are reported for comparison in **a**. Inset in **c** shows a magnification of the high frequency region. The numbers and corresponding filled symbols indicate selected frequency decades. **d** Arrhenius plot of the total conductivity under dry and humidified air, and dry and humidified 5% H_2 (in N_2).

Overall, the impedance spectroscopy measurements conducted under the various gas atmospheres confirm the results obtained from the conductivity measurements against the partial pressure of oxygen.

S5.3 Kramers-Kronig validation

The reliability of the measured impedance data was evaluated using Kramers-Kronig (KK) transformations. Kramers-Kronig validation ensures that the impedance response is a representation of a linear, time-invariant (i.e. the measured cell is in equilibrium) and casual system. KK relations relate the real and imaginary parts of the impedance spectrum to each other, and properly collected impedance data must obey these KK relations [43]. A plot of the KK residuals ($\Delta Z'_{KK}$, $\Delta Z''_{KK}$) arising from applying the KK transformations to the impedance data against the logarithm of the frequency shows whether the data set complies with the KK rules. Residuals randomly scattered around the frequency axis indicate that the system complies with the KK relations and therefore the effectiveness of the collected data [44]. On the other hand, a clear trace around the frequency axis, normally in the form of an oscillating trend, indicates that the data is corrupted. The *Lin-KK tool* software was employed to perform KK test on the collected impedance data [45]. KK residual plots at selected temperatures are reported in Figure S14.

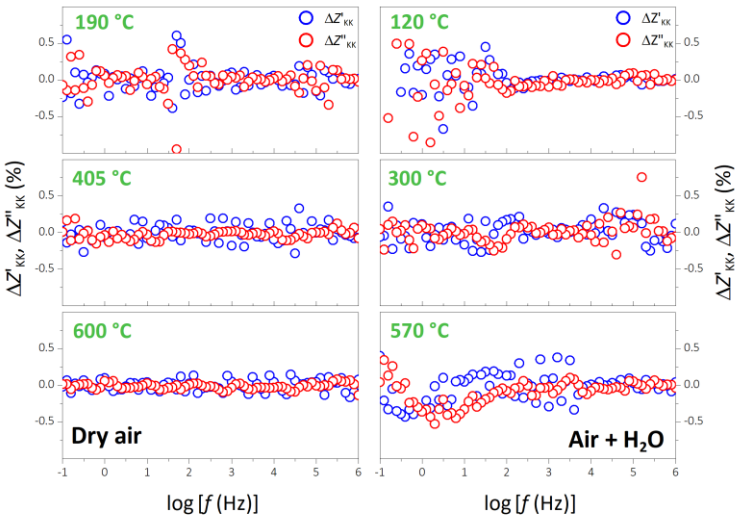

Figure S14. Residual plots obtained from the Kramers-Kronig tests conducted on the impedance data recorded under dry air and air + H_2O.

Randomly scattered KK residuals were obtained for both data sets measured under dry and humidified air at all temperatures. Similar plots were obtained for the impedance data collected under O_2, N_2 and 5% H_2 (in N_2). Therefore, KK test confirms the validity of the collected data.

S5.4 Equivalent circuit analysis

An equivalent circuit (EC) fitting procedure was employed to extract the individual bulk, grain boundary and electrode responses for the impedance data collected under dry and humidified air. The equivalent circuits depicted in Figure S15 were used to model the impedance data in dry air and air + H_2O.

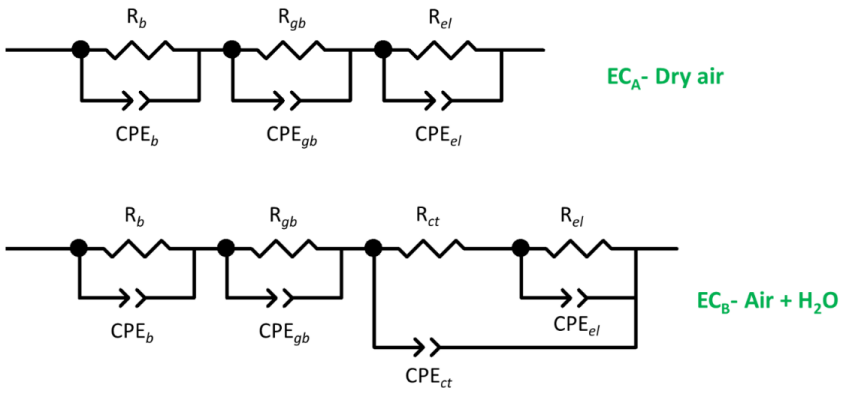

Figure S15. Equivalent circuits used to model the impedance data recorded in dry air (EC_A) and air + H_2O (EC_B). R indicates a resistor, while CPE is a constant phase element; the subscript *b* stands for bulk, *gb* for grain boundary, *el* for electrode and *ct* for charge transfer.

In these equivalent circuits, R indicates a resistor, while CPE is a constant phase element; the subscript *b* stands for bulk, *gb* for grain boundary, *el* for electrode and *ct* for charge transfer. The equivalent circuit EC_A was employed to model the data collected under dry air. Above 390 °C, the $(R\text{-}CPE)_b$ element for the bulk response is substituted by a series resistance, R_b, followed by the (R-CPE) elements for the grain boundary and electrode responses. EC fitting and deconvolution of the bulk and grain boundary conductivity was possible up to 655 °C. Above 670 °C the electrode response dominates the impedance data and every attempted model lead to unsatisfactorily results, with large errors and poor match between the calculated and observed complex impedance. The equivalent circuit EC_B was used for the impedance data collected under humidified air. For T > 300 °C, the $(R\text{-}CPE)_b$ element for the bulk response is substituted by a series resistance, R_b. The resistance R_{ct} gradually decreases as the temperature rises. Above 405 °C, the data can be modelled without any $(R\text{-}CPE)_{ct}$ element. Extraction of bulk and grain boundary resistivity values was possible up to 570 °C.

Above this temperature, the electrode polarisation resistance starts dominating the impedance, leading to increased errors in the bulk conductivity value determination.

Equivalent circuit fits at selected temperatures are presented in Figure S9, Figure S10 and Figure S11. A good match between the observed and calculated spectra is evident from the graphs. The validity of the equivalent circuit analysis can be further evaluated by inspection of the distribution of the EC residuals ($\Delta Z'_{EC}$, $\Delta Z''_{EC}$) versus the logarithm of the frequency. The residuals of a model which appropriately represents the observed data should be randomly distributed along the log(f) axis [44]. Selection of an incorrect model leads to a systematic distribution of the residuals, with a distinct oscillating trace with respect to the abscissa [46]. Figure S16 shows the EC residuals of some selected temperatures and evidences how the EC residuals are reasonably scattered along log(f). The good match between observed and calculated impedance data, and the random distribution of the EC residuals indicate that the employed equivalent circuit models adequately represent the collected data.

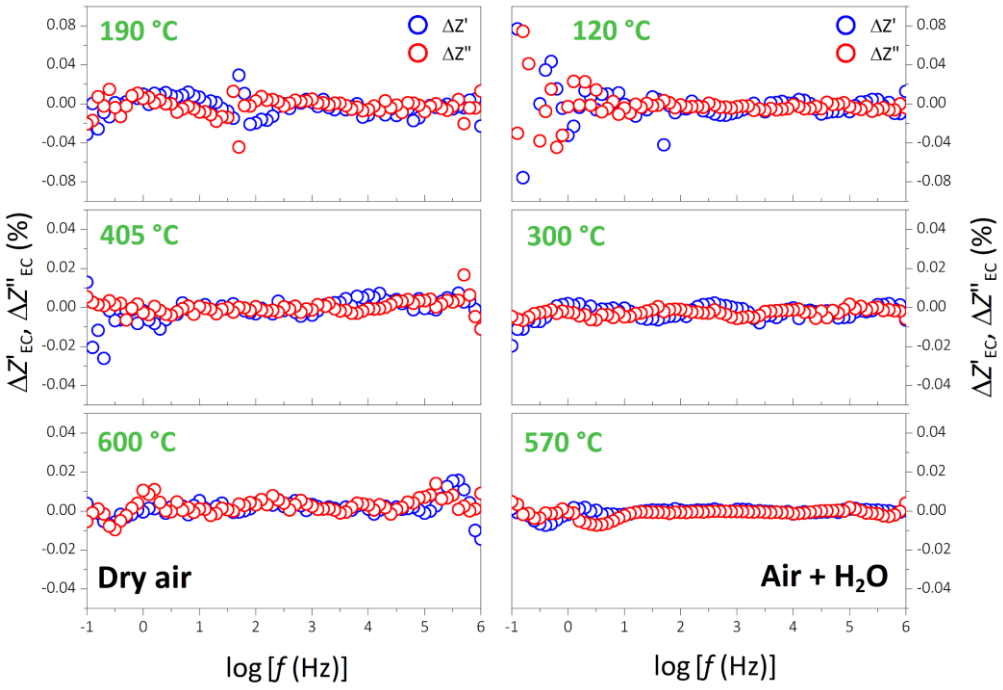

Figure S16. EC Residual plots of the equivalent circuit fitting procedure.

S5.5 Conductivity under fuel cell conditions

Total conductivity values at high temperatures were measured under the fuel cell conditions employed for the concentration cell experiments as described in the methods section. The Arrhenius plot in Figure S17 evidences that the fuel cell conductivity shows excellent agreement with the data obtained from impedance spectroscopy, thus validating the conductivity of the sample.

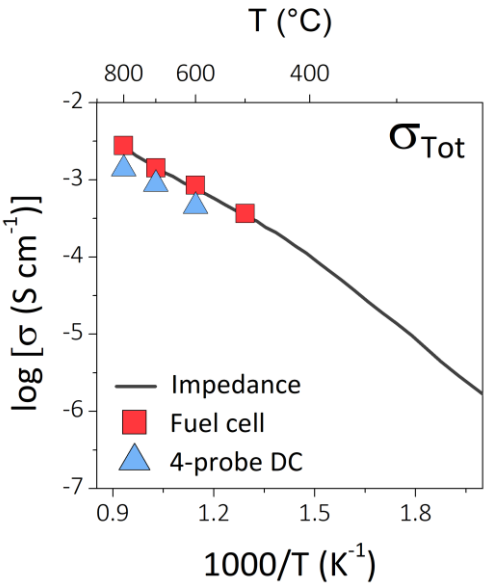

Figure S17. Arrhenius plot of the total conductivity of $Ba_7Nb_4MoO_{20}$ measured under fuel cell conditions (red squares) and obtained from four-probe direct current (DC) measurements (blue triangles). The conductivity from impedance spectroscopy measurements is also shown for comparison (grey line).

High temperature four-probe DC measurements (which do not contain any contribution from the electrolyte-electrode interface and only depend on the grain interior) taken in the pO_2 cell also agree well with the other sets of data, further confirming that the conductivity extracted from complex impedance is intrinsic to the sample [47, 48]. The slight discrepancy is due to the lower density of the porous sample employed for the pO_2 experiments (~ 70% of the theoretical density, compared to ~ 95% of the pellets for fuel cell and impedance testing) which obviously leads to lower conductivity values.

S6. Proton conductivity

$Ba_7Nb_4MoO_{20}$ shows an increase in conductivity when exposed to humidified air, revealing the presence of proton conduction. Proton conduction is influenced by the structural reorganisation of the oxygen fractional occupancies above ~ 300 °C.

The relative increase in conductivity under humidified air with respect to the conductivity in dry air can be calculated by

$$\Delta\sigma(\%) = \frac{\sigma_{Air + H_2O} - \sigma_{Dry\ air}}{\sigma_{Dry\ air}} \times 100$$

A plot of Δσ(%) calculated for the bulk, grain boundary and total conductivities is presented in Figure S18 and can be used to highlight the relative increase in conductivity under humidified air.

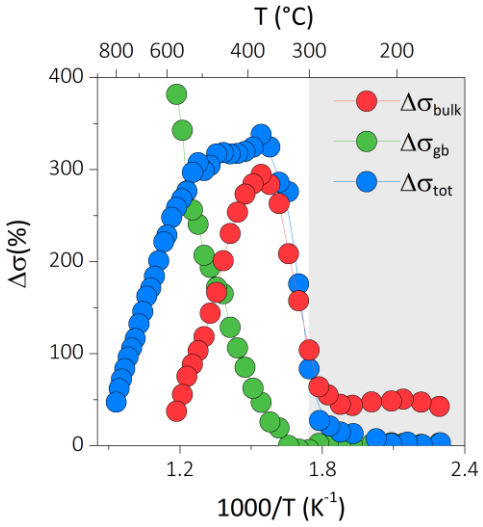

Figure S18. Relative difference plot between the conductivities recorded in dry and humidified air.

Below ~ 300 °C, the bulk conductivity in humidified air is about 50% higher than the conductivity in dry air, while the grain boundary and total conductivities show no or little increase. Above 300 °C, there is a large and sharp increase to about 300% in the bulk and total conductivity values under humidified atmosphere. The grain boundary conductivity also steeply increases for T > 300 °C.

The Arrhenius plot in Figure S19 shows the extracted bulk (σ_b) and grain boundary (σ_{gb}) conductivities in dry and humidified air. In $Ba_7Nb_4MoO_{20}$ the grain boundaries constitute the

most resistive part, mostly dominating the total resistivity of the material. The bulk conductivity in air + H_2O is higher than the bulk conductivity measured in dry air at most temperatures. As evidenced from the relative difference plot between the conductivity in air + H_2O and the conductivity in dry air presented in Figure S18, the increase in the bulk conductivity is more distinct above ~ 300 °C. The dry and humidified grain boundary conductivities are very similar below 300 °C; σ_{gb} in humidified air is higher than σ_{gb} in dry air above ~ 300 °C (Figure S19).

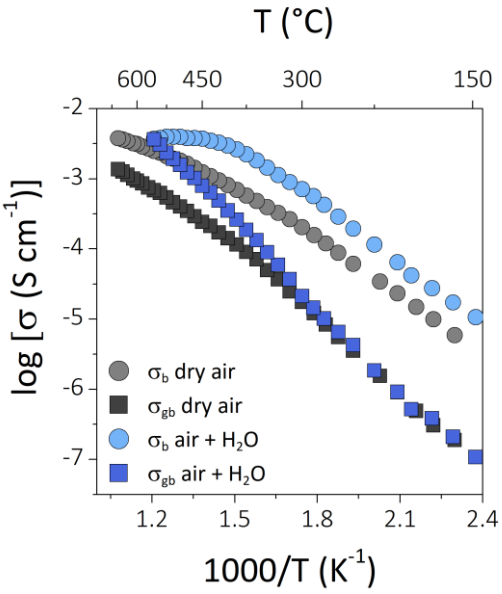

Figure S19. Arrhenius plot of the bulk and grain boundary conductivity of $Ba_7Nb_4MoO_{20}$ in dry ($pH_2O < 10^{-4}$ atm) and humidified air ($pH_2O \sim 0.021$ atm).

Figure S18 shows that whilst the bulk exhibits proton conductivity at all temperatures, proton conductivity is only observed in the grain boundary above ~ 350 °C. Below this temperature the proton conductivity is most likely hindered by structural distortions in the grain boundary region which leads to a decrease in proton mobility and potentially a depletion of protonic defects [49]. The ionic conduction in $Ba_7Nb_4MoO_{20}$ is correlated with the distribution of intrinsic oxygen vacancies along the palmierite-like layers. Above 300 °C the reorganisation of the oxygen fractional occupancies towards lower (average tetrahedral) coordination environments appears to alleviate the structural distortions in the grain boundary so that significant proton conductivity is observed in the grain boundary. This is apparent in Figure S10 where the grain boundary resistivity in humidified air decreases more rapidly with

increasing temperature than the bulk resistivity, as clearly evidenced by the reduction in the resolution of the grain boundary arc in the complex impedance plots.

Proton conduction in $Ba_7Nb_4MoO_{20}$ is further corroborated by impedance spectroscopy measurements in air + D_2O, which clearly show a reduction in conductivity due to the isotope effect (Figure 2d in the main manuscript). A plot of the ratio between the resistivity of the sample in air + D_2O and the values obtained in air + H_2O prior and after the measurements in heavy water shows that the resistivity in air + D_2O is ~ 1.3 – 1.4 times higher above 300 °C (Figure S20) and demonstrates that the transport is dominated by proton conduction above 400 °C.

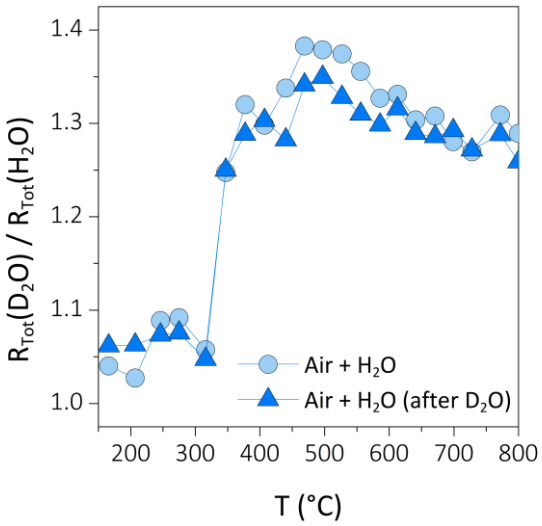

Figure S20. Plot of the ratio between the resistivity of the sample in air + D_2O and air + H_2O against the temperature.

The Arrhenius plot in Figure S21 shows a comparison between the bulk conductivities of $Ba_7Nb_4MoO_{20}$ and $Ba_3NbMoO_{8.5}$. $Ba_3NbMoO_{8.5}$ shows a reduction in conductivity on going from dry to humidified air atmosphere, suggesting that there is no proton conduction in this material [4, 50]. In the room temperature average crystal structure of $Ba_3NbMoO_{8.5}$, most of the oxide ions on the oxygen-vacant palmierite-like layer occupy the average octahedral O2 site (~ 55%). In $Ba_7Nb_4MoO_{20}$, only ~ 20% of the oxygen atoms occupy O2, with the majority of the oxygen atoms being on the average tetrahedral O1 site. The different oxygen/vacancy distributions in $Ba_3NbMoO_{8.5}$ most likely create higher coordination environments which are unfavourable for proton transport along the palmierite-like layers. This is further

corroborated by the fact that the proton conductivity increases markedly in $Ba_7Nb_4MoO_{20}$ with the rearrangement of the O1/O2 fractional occupancies.

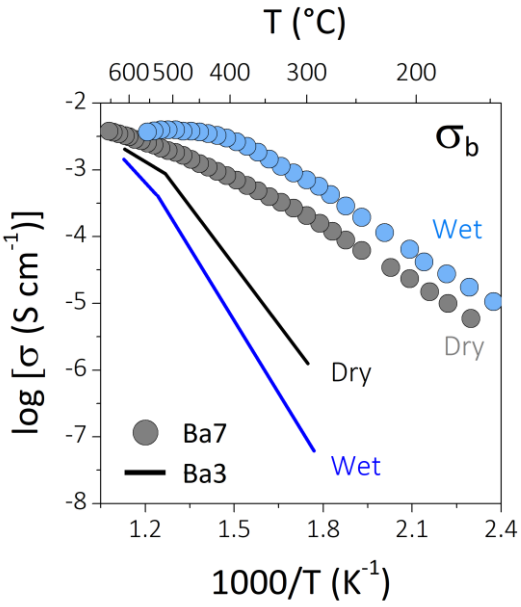

Figure S21. Arrhenius plot of the bulk conductivity of $Ba_7Nb_4MoO_{20}$ (Ba7) and $Ba_3NbMoO_{8.5}$ (Ba3) under dry and humidified (wet) air.

Generally, the total conductivity (σ) in a typical oxide material is the sum of electronic and ionic components. In the case of $Ba_7Nb_4MoO_{20}$, the ionic component arises from migration of oxide ions and protons, therefore:

$$\sigma = \sigma_{O^{2-}} + \sigma_H + \sigma_e$$

which implies the following relationship for the transport numbers of the different species

$$t_{O^{2-}} + t_H + t_e = 1$$

Concentration cell, impedance spectroscopy and conductivity against pO_2 measurements evidence that $Ba_7Nb_4MoO_{20}$ presents predominant ionic conduction with negligible electronic conductivity, thus resulting in $\sigma_e \sim 0$ and $t_e \sim 0$. Therefore

$$\sigma = \sigma_{O^{2-}} + \sigma_H$$

$$t_{O^{2-}} + t_H = 1$$

The oxide ion transport number in dry conditions was obtained from the concentration cell experiments, as reported in Figure 1c. Assuming that the proton conduction has no effect on the other charge carriers, the proton transport number can be estimated from the values of the total conductivity in dry and humidified atmosphere [51]. In dry air atmosphere, the conductivity σ_{Dry} of $Ba_7Nb_4MoO_{20}$ is purely oxygen ionic ($t_{O^{2-}} \sim 1$), therefore

$$\sigma_{Dry} = \sigma_{O^{2-}}$$

Since any electronic component is negligible, any additional contribution in humidified (or hydrogen-richer) atmosphere is only due to an extra protonic component, meaning that the conductivity σ_{H_2O} in air + H_2O is given by

$$\sigma_{H_2O} = \sigma_{O^{2-}} + \sigma_H$$

from which it is possible to obtain

$$\sigma_H = \sigma_{H_2O} - \sigma_{Dry}$$

Hence the proton transport number t_H can be calculated according to:

$$t_H = \frac{\sigma_H}{\sigma_{H_2O}}$$

In dry/oxidising conditions, the oxygen ionic conductivity is predominant with $t_{O^{2-}} \sim 1$. Under humidified (hydrogen-richer) atmospheres, there is an additional and significant protonic component, which becomes dominant above ~ 300 °C, simultaneously with the structural rearrangement of the oxygen O1/O2 fractional occupancies. The estimated proton transport number in humidified air and humidified 5% H_2 (in N_2) presented in Figure S22 evidences a steep increase above ~ 300 °C, from $t_H \sim 0.25$ (air) and 0.30 (5% H_2 (in N_2)) (therefore $t_{O^{2-}} \sim 0.75$ and 0.70 under the same conditions) at 270 °C to $t_H \sim 0.80$ (air) and 0.85 (5% H_2 (in N_2)) ($t_{O^{2-}} \sim 0.20$ and 0.15 under the same conditions) at 510 °C.

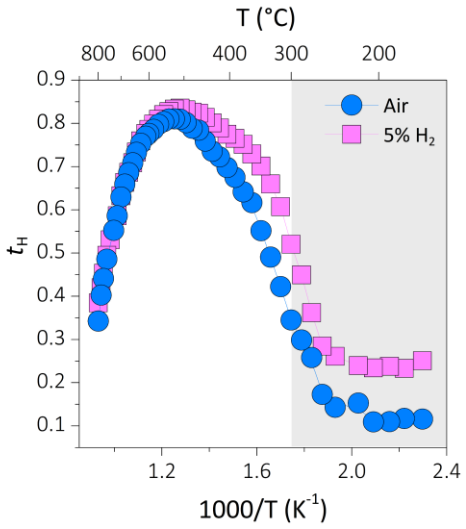

Figure S22. Proton transport number calculated from the total conductivity values in humidified air and humidified 5% H_2 (in N_2).

Proton and oxide ion transport compete against each other [52], since they are enabled by the same intrinsic oxygen defects distributed along the palmierite-like layers, but are not mutually exclusive [49]. Under humidified atmosphere, protonic and oxygen defects clearly coexist, enabling both kinds of ionic transport (such as in the case of $BaZr_{0.1}Ce_{0.7}Y_{0.1}Yb_{0.1}O_{3-\delta}$ [53] and of triple conducting $PrBa_{0.5}Sr_{0.5}Co_{1.5}Fe_{0.5}O_{5+\delta}$ [54]); whether proton or oxide ion transport dominates depends on the value of pH_2O/pO_2 and temperature (Figure S22). $Ba_7Nb_4MoO_{20}$ exhibits significant oxide ion conductivity in dry/oxidising conditions, simultaneously with high levels of proton conductivity under humidified atmospheres.

Since oxide ion and proton transport share common features, ionic conducting oxides can show oxide ion conductivity and at the same time have affinity for chemical diffusion of water [49]. However, not all oxide ionic conductors present protonic components and/or show significant proton transport at specific conditions [4, 55, 51, 56]. At the same time, most proton conductors exhibit *p*-type electronic conductivity under dry/oxidising conditions [28, 57, 58]. Materials that show considerable conductivity for both oxide ions and protons have been defined as dual-ion conductors [35], and $Ba_7Nb_4MoO_{20}$ can be considered to belong to this group. $Ba_7Nb_4MoO_{20}$ is the first hexagonal derivative to show dual-ion conduction, with significant oxide ion conduction in dry oxidising/reducing conditions and high proton conductivity in humidified atmospheres.

S7. Water uptake

Proton uptake in $Ba_7Nb_4MoO_{20}$ and $Ba_3NbMoO_{8.5}$ was investigated by thermogravimetric analysis, upon cooling the samples in equilibrium isotherms. Details for the measurements of $Ba_7Nb_4MoO_{20}$ are reported in the Methods section in the main manuscript. Measurements on $Ba_3NbMoO_{8.5}$ followed a similar procedure, but the sample was only heated to 600 °C since the phase is not stable between 650 °C and 1000 °C [4, 59]. Results from the TGA experiment for $Ba_7Nb_4MoO_{20}$ are reported in Figure 5a in the manuscript, while the water uptake of $Ba_3NbMoO_{8.5}$ is presented in Figure S23. The proton concentration as a function of the temperature for both compounds is reported in Figure S24. For $Ba_7Nb_4MoO_{20}$, the weight increase at room temperature corresponds to ~ 0.80 H_2O molecules per formula unit, while the weight increase of $Ba_3NbMoO_{8.5}$ corresponds to ~ 0.20 molecules of water. The number of molecules of water per formula unit of $Ba_7Nb_4MoO_{20}$ obtained from the TGA measurements is 80% of the theoretical solubility limit and consistent with the value of one oxygen vacancy per formula unit. The value for $Ba_3NbMoO_{8.5}$ is consistent with 0.5 oxygen vacancy per formula unit. Analogous water concentrations have been reported for other perovskite-related systems with intrinsic oxygen vacancies such as $Ba_2In_2O_5$-based compounds [60, 61], $Ba_2Sc_2O_5$ [62], $Sr_6Ta_2O_{11}$ [63], $Ba_4M_2O_9$ (with M = Nb, Ta) [64].

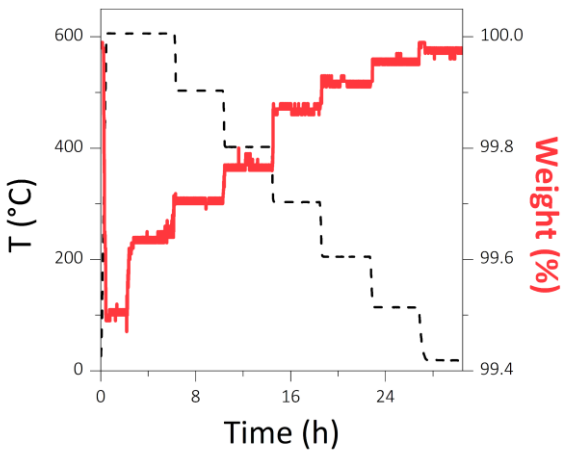

Figure S23. Water uptake of $Ba_3NbMoO_{8.5}$ measured by equilibrium isotherms with thermogravimetric analysis under humidified air (pH_2O ~ 0.021 atm).

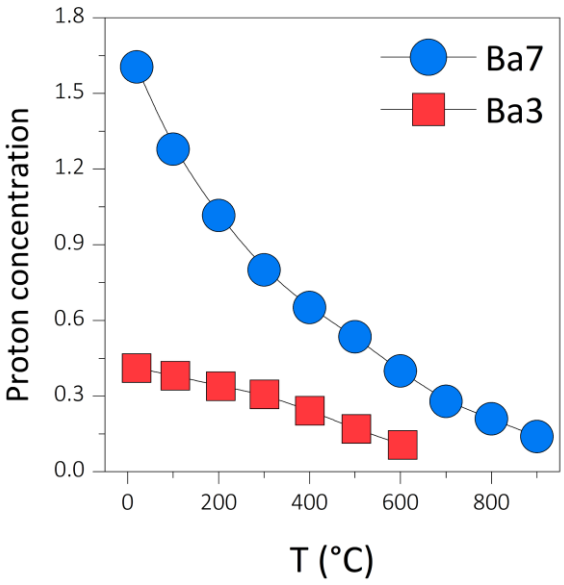

Figure S24. The Proton concentration of $Ba_7Nb_4MoO_{20}$ (Ba7) and $Ba_3NbMoO_{8.5}$ (Ba3) obtained from thermogravimetric analysis.

In order to evaluate the thermodynamics of proton uptake, the defect structure of $Ba_7Nb_4MoO_{20}$ was described by employing the extended Kröger-Vink notation for defects in inherently defective sub-lattices as defined by Norby [65]. Hydration of $Ba_7Nb_4MoO_{20}$ most likely occurs on the intrinsically oxygen-vacant palmierite-like layers with general composition $Ba_3M_2O_8$. The palmierite structure is derived from the 9R polytype ($Ba_3M_2O_9$) by replacement of the [BaO_3] cubic layer by an oxygen-deficient layer of composition [BaO_2] [66]; there is one oxygen vacancy per palmierite pseudo-cubic [BaO_2] layer. In $Ba_7Nb_4MoO_{20}$, the palmierite-like layers present a disordered distribution of filled and vacant oxygen sites due to the competitive occupation of O1/O2, but still contains only one oxygen vacancy per layer. Therefore, the perfect oxygen site is statistically occupied 8/9 with an oxide ion and 1/9 with a vacancy; in the extended notation this site can be denoted as $\frac{8}{9}O$. Following the approach by Norby, the oxide ion and its effective charge can be denoted as $O_{\frac{8}{9}O}^{\frac{2}{9}\prime}$, while the oxygen vacancy and its charge as $V_{\frac{8}{9}O}^{\frac{16}{9}\bullet}$.

The reaction for the dissociative absorption of water can be written as:

$$H_2O\ (g)\ +\ V_{\frac{8}{9}O}^{\frac{16}{9}\bullet}\ +\ O_{\frac{8}{9}O}^{\frac{2}{9}\prime}\ \leftrightarrow\ 2OH_{\frac{8}{9}O}^{\frac{7}{9}\bullet}$$

And the associated equilibrium constant, K_W

$$K_W = \frac{[OH_{\frac{8}{9}O}^{\frac{7}{9}\bullet}]^2}{pH_2O\ [V_{\frac{8}{9}O}^{\frac{16}{9}\bullet}]\ [O_{\frac{8}{9}O}^{\frac{2}{9}\prime}]} = exp\ \frac{\Delta S^0}{R} exp \frac{\Delta H^0}{RT}$$

The electroneutrality and site occupancy conditions are

$$7\ [OH_{\frac{8}{9}O}^{\frac{7}{9}\bullet}]\ +\ 16\ [V_{\frac{8}{9}O}^{\frac{16}{9}\bullet}]\ =\ 2\ [O_{\frac{8}{9}O}^{\frac{2}{9}\prime}]$$

$$[OH_{\frac{8}{9}O}^{\frac{7}{9}\bullet}]\ +\ [V_{\frac{8}{9}O}^{\frac{16}{9}\bullet}]\ +\ [O_{\frac{8}{9}O}^{\frac{2}{9}\prime}]\ =\ 9$$

These conditions can be used to express the equilibrium constant in terms of proton concentration:

$$K_W = \frac{4[OH_{\frac{8}{9}O}^{\frac{7}{9}\bullet}]^2}{pH_2O\ (32\ -\ 18\ [OH_{\frac{8}{9}O}^{\frac{7}{9}\bullet}]\ +\ [OH_{\frac{8}{9}O}^{\frac{7}{9}\bullet}]^2)}$$

Proton concentrations are measured from the thermogravimetric analysis and are employed for the determination of K_w (Figure 5b in the manuscript). The linear fit to the graph (following the van't Hoff relationship) yields the enthalpy (ΔH^0) and entropy (ΔS^0) of the hydration reaction for $Ba_7Nb_4MoO_{20}$.

The calculation of K_W for $Ba_3NbMoO_{8.5}$ follows a similar approach. For $Ba_3NbMoO_{8.5}$ there is 0.5 oxygen vacancy per palmierite pseudo-cubic [$BaO_{2.5}$] layer. Therefore, the oxygen site is denoted as $\frac{17}{18}O$, and the oxide ion and its effective charge are denoted as $O_{\frac{17}{18}O}^{\frac{1}{9}\prime}$, while the oxygen vacancy and its charge is given as $V_{\frac{17}{18}O}^{\frac{17}{9}\bullet}$.

The reaction for the dissociative absorption of water can be written as:

$$H_2O_{(g)} + V_{\frac{17}{18}O}^{\frac{17}{9}\bullet} + O_{\frac{17}{18}O}^{\frac{1}{9}\prime} \leftrightarrow 2OH_{\frac{17}{18}O}^{\frac{8}{9}\bullet}$$

And the associated equilibrium constant, K_W

$$K_W = \frac{[OH_{\frac{17}{18}O}^{\frac{8}{9}\bullet}]^2}{pH_2O\,[V_{\frac{17}{18}O}^{\frac{17}{9}\bullet}]\,[O_{\frac{17}{18}O}^{\frac{1}{9}\prime}]}$$

The electroneutrality and site occupancy conditions are

$$8\,[OH_{\frac{17}{18}O}^{\frac{8}{9}\bullet}] + 17\,[V_{\frac{17}{18}O}^{\frac{17}{9}\bullet}] = [O_{\frac{17}{18}O}^{\frac{1}{9}\prime}]$$

$$[OH_{\frac{17}{18}O}^{\frac{8}{9}\bullet}] + [V_{\frac{17}{18}O}^{\frac{17}{9}\bullet}] + [O_{\frac{17}{18}O}^{\frac{1}{9}\prime}] = 9$$

The equilibrium constant in terms of proton concentration:

$$K_W\,(Ba3) = \frac{4[OH_{\frac{17}{18}O}^{\frac{8}{9}\bullet}]^2}{pH_2O\,(17 - 18\,[OH_{\frac{17}{18}O}^{\frac{8}{9}\bullet}] + [OH_{\frac{17}{18}O}^{\frac{8}{9}\bullet}]^2)}$$

For $Ba_3NbMoO_{8.5}$, hydration enthalpy and entropy values are ΔH^0 = -10 kJ mol^{-1} and ΔS^0 = -17 J K $^{-1}$ for T < 300 °C; above 300 °C, there is a gradual change in slope with ΔH^0 = -44 kJ mol^{-1} and ΔS^0 = -61 J K $^{-1}$ mol^{-1} at high temperatures.

S8. Stability

The Arrhenius plot of the total conductivity measured in dry air after measurements in each of the various gases (Air + H_2O, O_2, N_2 and 5% H_2 (in N_2)) evidences how the electrical properties of $Ba_7Nb_4MoO_{20}$ are stable in cycling through the different atmospheres (Figure S25a).

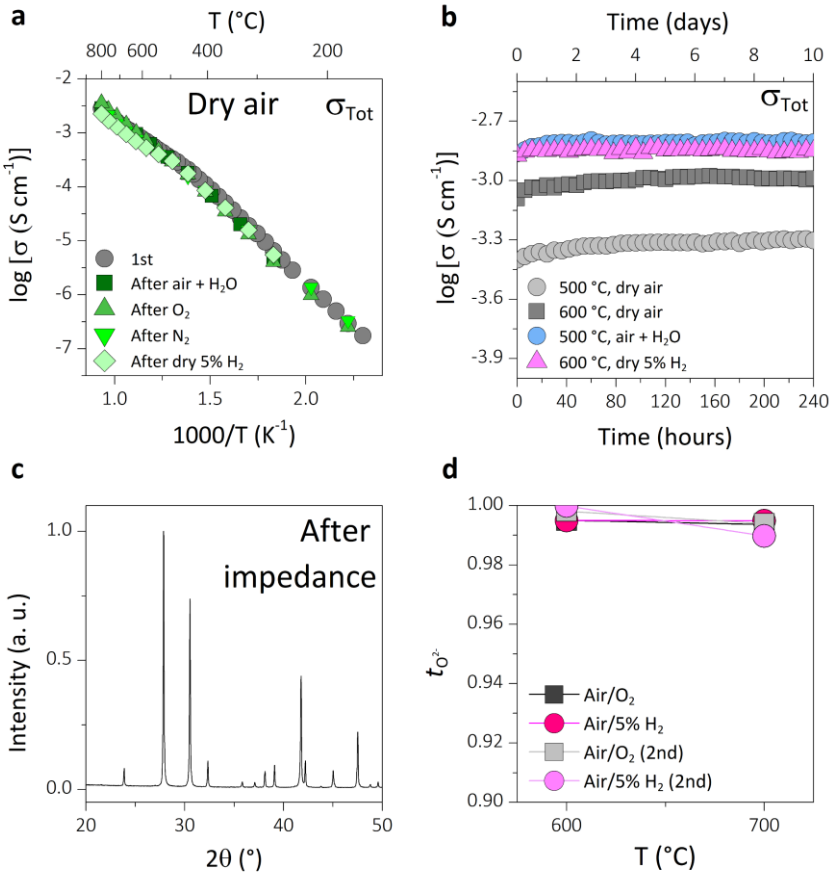

Figure S25. a Arrhenius plot of the total conductivity in dry air measured after impedance spectroscopy measurements performed in the various gases. **b** Variation of the total conductivity with time under different atmospheres. **c** XRD pattern of the sample collected after completing all the impedance spectroscopy tests. **d** Oxygen transport numbers in air/O_2 and air/5% H_2 obtained from a second set of concentration cell experiments. Results from the first measurements are reported for comparison.

The conductivity of $Ba_7Nb_4MoO_{20}$ is also stable after several days of measurements (Figure S25b). Oxide ion conductors based on doped $Bi_4V_2O_{11}$ (BIMEVOX) and bismuth oxide derivatives are highly unstable, and typically present a degradation in conductivity (even after first use) due to different order/disorder structural transitions caused by prolonged annealing

and/or heating/cooling cycles [67, 68, 69]. On the contrary, $Ba_7Nb_4MoO_{20}$ does not show any evidence of conductivity degradation, nor phase changes or formation of impurities (as seen from an XRD pattern collected on the sample after all the impedance spectroscopy stability tests, Figure S25c), following numerous heating/cooling and annealing cycles under various atmospheres. Concentration cell experiments performed subsequently to the first set of measurements also demonstrate that the ionic conduction is fully reversible (Figure S25d). These results further confirm the excellent electrical and phase stability of $Ba_7Nb_4MoO_{20}$.

S9. Neutron diffraction study of $Ba_7Nb_4MoO_{20}$

S9.1 Rietveld refinement

Garcia-González *et al* reported $Ba_7Nb_4MoO_{20}$ as a 7H hexagonal perovskite polytype with stacking sequence *hhchhcc* [1]. The authors described the structure as an ordered intergrowth of the 12R perovskite $Ba_4M_3O_{12}$ (where M denotes either Mo or Nb) units and palmierite $Ba_3M_2O_8$ units. Intrinsic anionic vacancies are accommodated within the palmierite $Ba_3M_2O_8$ layers, which are interspaced from the 12R blocks by a plane of empty cationic sites. Both types of structural units are isolated by the ordered cationic vacancies and stacked in a hexagonal disposition with respect to the other.

Variable temperature neutron diffraction data were collected on the high-resolution D2B diffractometer at the Institute Laue-Langevin (ILL) to further investigate any correlation between the electrical properties and crystal structure of $Ba_7Nb_4MoO_{20}$. Rietveld refinement of the variable temperature neutron powder diffraction data of $Ba_7Nb_4MoO_{20}$ was performed using the GSAS/EXPGUI package [70]. The background was fitted by the Chebyschev polynomial function, and the peak shapes were modelled using a pseudo-Voigt function. The structure by Garcia-González *et al* [1] was employed as a starting model for the Rietveld analysis. Anisotropic displacement parameters (U_{ij}) were constrained to be the same for the Ba and Mo/Nb cations, while the ones for the oxygen atoms were freely refined, resulting in agreement indexes R_{wp} = 9.71%, R_p = 8.82% and χ^2 = 2.71 for the data collected at 50 °C. Large U_{11}, U_{22} thermal displacement parameters were obtained for the apical tetrahedral oxygen atom O1 within the palmierite layers, clearly suggesting oxygen disorder on the *ab* plane, as previously evidenced by Garcia-González *et al* [1]. Attempts to model this disorder by splitting the O1 site from Wyckoff position 2*d* to 6*i* and using a single isotropic displacement parameter (U_{iso}) still resulted in large unrealistic thermal displacement values. The use of difference Fourier maps allowed the identification of missing neutron scattering density, unaccounted for by the model by Garcia-González *et al*, in proximity of the apical tetrahedral oxygen atom (O1), at Wyckoff position 3*e* (½, 0, 0) (Figure 4a in manuscript). Difference Fourier maps also revealed missing scattering density at 2*d* (⅓, ⅔, ~0.19), in the empty cationic sites separating the palmierite and 12R layers (Figure S26).

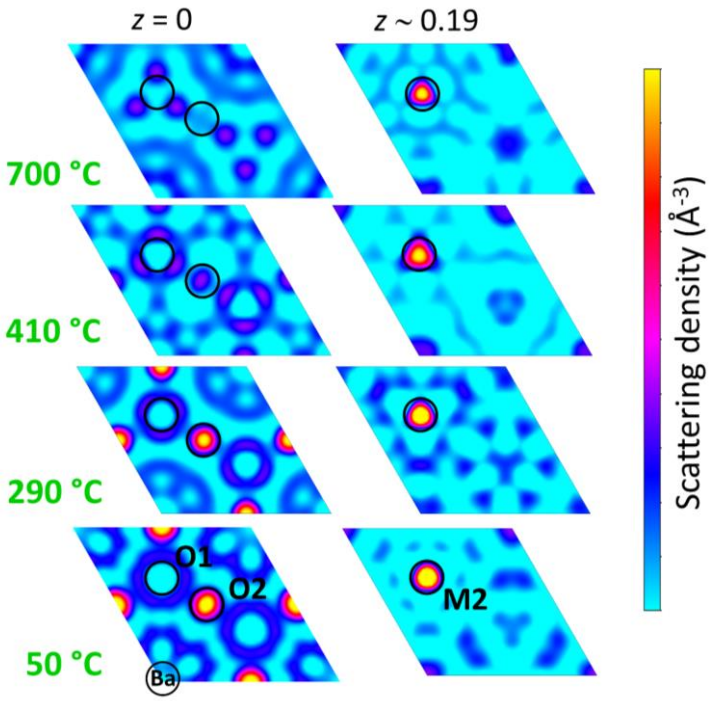

Figure S26. Difference Fourier maps seen along the [001] direction at $z = 0$ and $z \sim 0.19$ at selected temperatures. The maps were calculated from the Rietveld fit to the neutron data according to the model proposed by Garcia-González *et al* (ref. 1) and clearly evidence unaccounted neutron scattering density at O2 and M2. There is no significant residual scattering density at O2 above 500 °C, evidencing that the site is unoccupied at high temperatures.

A structural model with an extra oxygen atom at position 3*e* (O2) and a metal atom at 2*d* (M2) was constructed to take into account the missing scattering density (Table S2 and Figure 4b in the manuscript). The Rietveld fit to this model resulted in excellent agreement between the calculated and observed patterns for all temperatures (Figure S27), with good *R*-factors and low χ^2 values (Table S2).

No significant residual neutron scattering density is detected in the difference Fourier maps calculated from the proposed model. There is no evidence of peak splitting or superstructure peaks, and the $P\bar{3}m1$ symmetry space group is observed over the whole temperature range.

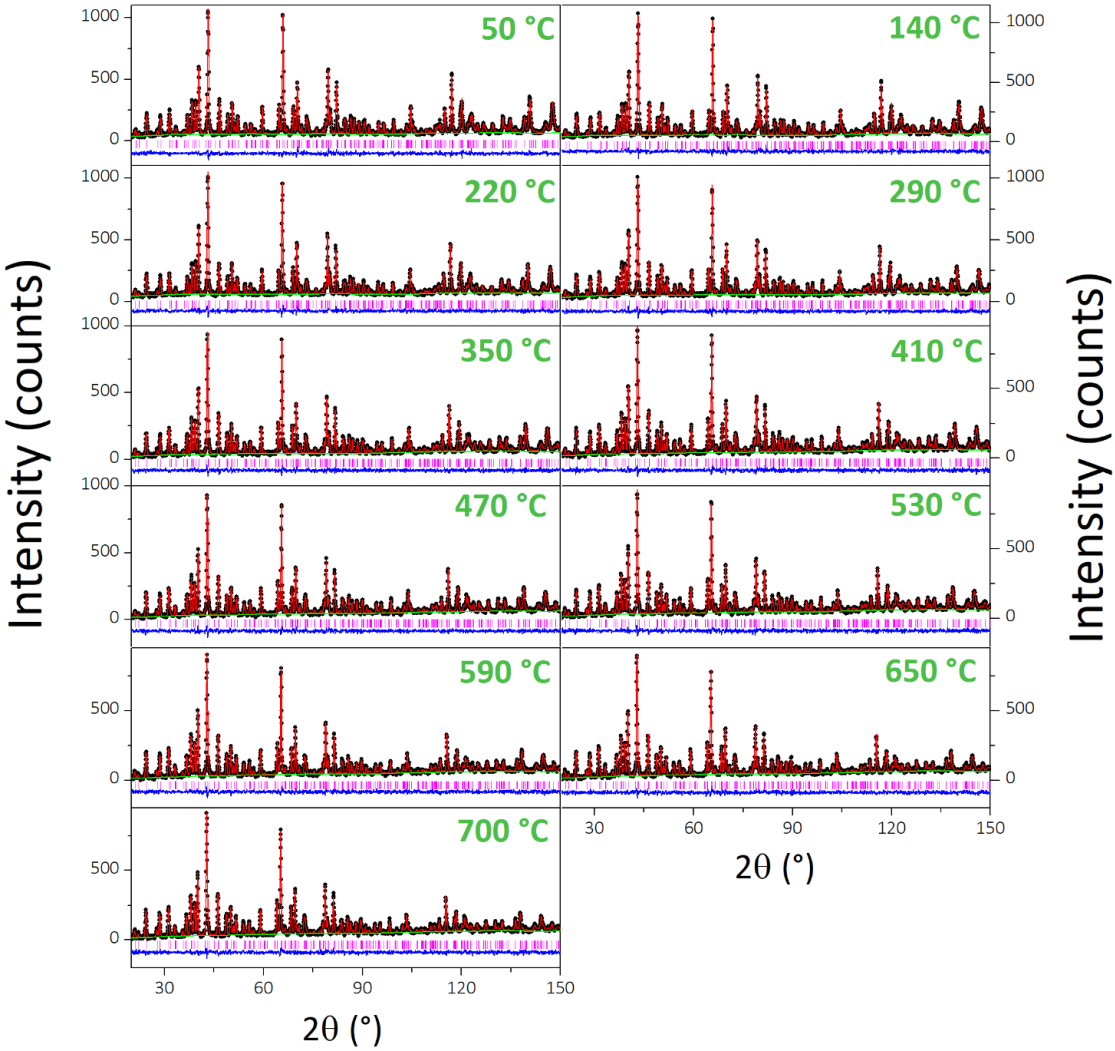

Figure S27. Rietveld refinement fit to the variable temperature neutron diffraction data. Black dots indicate the observed data, the red line the Rietveld fit, the blue line the difference between the observed and calculated patterns, the green line the background function, and the pink bars the reflection positions.

Table S2. Refined atomic parameters from Rietveld fit of the variable temperature neutron diffraction data of $Ba_7Nb_4MoO_{20}$ recorded on the D2B diffractometer. Data were refined in the space group $P\bar{3}m1$. U_{ij} indicates anisotropic thermal displacement parameters (in Å^2). U_{13} and U_{23} are zero due to the symmetry of the system. O1 and O2 were refined with an isotropic thermal displacement parameter, U_{iso} (in Å^2).

			50 °C	**140 °C**	**220 °C**	**290 °C**	**350 °C**	**410 °C**	**470 °C**	**530 °C**	**590 °C**	**650 °C**	**700 °C**
	***a* (Å)**		5.86578(4)	5.87138(6)	5.87721(5)	5.8836(1)	5.88943(6)	5.89460(6)	5.90008(6)	5.90546(7)	5.91079(7)	5.91639(7)	5.92104(8)
	***c* (Å)**		16.5428(2)	16.5535(3)	16.5627(3)	16.5907(4)	16.6126(3)	16.6252(3)	16.6362(3)	16.6481(3)	16.6599(3)	16.6719(3)	16.6832(4)
	***V* (Å^3)**		492.940(8)	494.19(1)	495.45(1)	497.38(2)	499.02(1)	500.27(1)	501.54(1)	502.81(1)	504.07(2)	505.39(2)	506.53(2)
			50 °C	**140 °C**	**220 °C**	**290 °C**	**350 °C**	**410 °C**	**470 °C**	**530 °C**	**590 °C**	**650 °C**	**700 °C**
Ba1	**(0,0,0)**	$U_{11} = U_{22}$	0.0176(6)	0.0202(7)	0.0214(7)	0.0230(8)	0.0259(8)	0.0279(8)	0.0266(8)	0.0285(8)	0.0295(9)	0.0309(9)	0.0330(9)
	1*a*	U_{33}	0.0180(2)	0.0190(2)	0.023(1)	0.022(2)	0.019(1)	0.022(2)	0.022(2)	0.022(2)	0.021(2)	0.022(2)	0.023(2)
		U_{12}	0.0088(3)	0.0101(4)	0.0107(4)	0.0115(4)	0.0130(4)	0.0139(4)	0.0133(4)	0.0143(4)	0.0147(4)	0.0155(5)	0.0165(5)
Ba2	**(⅓,⅔,*z*)**	***z***	0.8278(4)	0.8284(4)	0.8289(5)	0.8271(5)	0.8262(4)	0.8246(4)	0.8241(4)	0.8244(4)	0.8243(4)	0.8231(4)	0.8236(4)
	2*d*	$U_{11} = U_{22}$	0.0176(6)	0.0202(7)	0.0214(7)	0.0230(8)	0.0259(8)	0.0279(8)	0.0266(8)	0.0285(8)	0.0295(9)	0.0309(9)	0.0330(9)
		U_{33}	0.0180(2)	0.0190(2)	0.023(1)	0.022(2)	0.019(1)	0.022(2)	0.022(2)	0.022(2)	0.021(2)	0.022(2)	0.023(2)
		U_{12}	0.0088(3)	0.0101(4)	0.0107(4)	0.0115(4)	0.0130(4)	0.0139(4)	0.0133(4)	0.0143(4)	0.0147(4)	0.0155(5)	0.0165(5)
Ba3	**(0,0,*z*)**	***z***	0.2789(4)	0.2792(5)	0.2783(6)	0.2773(5)	0.2788(5)	0.2792(5)	0.2797(5)	0.2798(5)	0.2806(5)	0.2818(5)	0.2815(5)
	2*c*	$U_{11} = U_{22}$	0.0176(6)	0.0202(7)	0.0214(7)	0.0230(8)	0.0259(8)	0.0279(8)	0.0266(8)	0.0285(8)	0.0295(9)	0.0309(9)	0.0330(9)
		U_{33}	0.0180(2)	0.0190(2)	0.023(1)	0.022(2)	0.019(1)	0.022(2)	0.022(2)	0.022(2)	0.021(2)	0.022(2)	0.023(2)
		U_{12}	0.0088(3)	0.0101(4)	0.0107(4)	0.0115(4)	0.0130(4)	0.0139(4)	0.0133(4)	0.0143(4)	0.0147(4)	0.0155(5)	0.0165(5)

Table S2. Continued

			50 °C	140 °C	220 °C	290 °C	350 °C	410 °C	470 °C	530 °C	590 °C	650 °C	700 °C
Ba4	**(⅓,⅔,*z*)**	***z***	0.5769(4)	0.5775(5)	0.5775(5)	0.5767(5)	0.5760(5)	0.5758(5)	0.5755(5)	0.5751(5)	0.5750(5)	0.5755(5)	0.5763(5)
	2*d*	$U_{11} = U_{22}$	0.0176(6)	0.0202(7)	0.0214(7)	0.0230(8)	0.0259(8)	0.0279(8)	0.0266(8)	0.0285(8)	0.0295(9)	0.0309(9)	0.0330(9)
		U_{33}	0.0180(2)	0.0190(2)	0.023(1)	0.022(2)	0.019(1)	0.022(2)	0.022(2)	0.022(2)	0.021(2)	0.022(2)	0.023(2)
		U_{12}	0.0088(3)	0.0101(4)	0.0107(4)	0.0115(4)	0.0130(4)	0.0139(4)	0.0133(4)	0.0143(4)	0.0147(4)	0.0155(5)	0.0165(5)
M1	**(⅓,⅔,*z*)**	***z***	0.0922(3)	0.0912(4)	0.0905(5)	0.0908(4)	0.0943(4)	0.0939(4)	0.0943(3)	0.0947(4)	0.0948(4)	0.0948(4)	0.0948(4)
	2*d*	**Fraction**	0.899(3)	0.884(3)	0.863(4)	0.875(3)	0.897(3)	0.915(3)	0.934(3)	0.931(3)	0.940(3)	0.947(3)	0.949(3)
		$U_{11} = U_{22}$	0.0102(5)	0.0131(6)	0.0141(6)	0.0161(7)	0.0160(6)	0.0166(6)	0.0190(6)	0.0186(7)	0.0220(7)	0.0219(7)	0.0228(8)
		U_{33}	0.028(2)	0.032(2)	0.032(1)	0.031(2)	0.024(2)	0.024(2)	0.023(2)	0.025(2)	0.023(2)	0.025(2)	0.024(20
		U_{12}	0.0018(2)	0.0065(2)	0.0070(3)	0.0081(3)	0.0080(3)	0.0083(3)	0.0095(3)	0.0093(3)	0.0110(4)	0.0155(5)	0.0114(4)
M2	**(⅓,⅔,*z*)**	***z***	0.1954(2)	0.1926(2)	0.194(1)	0.193(2)	0.193(2)	0.191(3)	0.191(4)	0.194(3)	0.192(4)	0.196(5)	0.198(5)
	2*d*	**Fraction**	0.101(3)	0.116(3)	0.137(4)	0.125(3)	0.103(3)	0.085(3)	0.066(3)	0.069(3)	0.060(3)	0.053(3)	0.051(3)
		$U_{11} = U_{22}$	0.0102(5)	0.0131(6)	0.0141(6)	0.0161(7)	0.0160(6)	0.0166(6)	0.0190(6)	0.0186(7)	0.0220(7)	0.0219(7)	0.0228(8)
		U_{33}	0.028(2)	0.032(2)	0.032(1)	0.031(2)	0.024(2)	0.024(2)	0.023(2)	0.025(2)	0.023(2)	0.025(2)	0.024(20
		U_{12}	0.0018(2)	0.0065(2)	0.0070(3)	0.0081(3)	0.0080(3)	0.0083(3)	0.0095(3)	0.0093(3)	0.0110(4)	0.0155(5)	0.0114(4)
M3	**(⅓,⅔,*z*)**	***z***	0.3510(3)	0.3515(3)	0.3510(4)	0.3507(3)	0.3508(3)	0.3493(3)	0.3495(3)	0.3501(1)	0.3498(3)	0.3499(3)	0.3499(3)
	2*d*	$U_{11} = U_{22}$	0.0102(5)	0.0131(6)	0.0141(6)	0.0161(7)	0.0160(6)	0.0166(6)	0.0190(6)	0.0186(7)	0.0220(7)	0.0219(7)	0.0228(8)
		U_{33}	0.028(2)	0.032(2)	0.032(1)	0.031(2)	0.024(2)	0.024(2)	0.023(2)	0.025(2)	0.023(2)	0.025(2)	0.024(20
		U_{12}	0.0018(2)	0.0065(2)	0.0070(3)	0.0081(3)	0.0080(3)	0.0083(3)	0.0095(3)	0.0093(3)	0.0110(4)	0.0155(5)	0.0114(4)

Table S2. Continued

			50 °C	140 °C	220 °C	290 °C	350 °C	410 °C	470 °C	530 °C	590 °C	650 °C	700 °C
M4	**(0,0,½)**	$U_{11} = U_{22}$	0.0176(6)	0.0131(6)	0.0141(6)	0.0161(7)	0.0160(6)	0.0166(6)	0.0190(6)	0.0186(7)	0.0220(7)	0.0219(7)	0.0228(8)
	1*b*	U_{33}	0.0180(2)	0.032(2)	0.032(1)	0.031(2)	0.024(2)	0.024(2)	0.023(2)	0.025(2)	0.023(2)	0.025(2)	0.024(20
		U_{12}	0.0088(3)	0.0065(2)	0.0070(3)	0.0081(3)	0.0080(3)	0.0083(3)	0.0095(3)	0.0093(3)	0.0110(4)	0.0155(5)	0.0114(4)
O1	**(x,$\bar{x}$,z)**	***x***	0.357(2)	0.350(3)	0.361(2)	0.363(2)	0.360(2)	0.364(2)	0.362(2)	0.364(2)	0.364(2)	0.368(1)	0.366(2)
	6*i*	***z***	-0.0162(6)	-0.0165(4)	-0.0153(5)	-0.0154(5)	-0.0149(6)	-0.0141(5)	-0.0140(5)	-0.0134(5)	-0.0137(6)	-0.0142(6)	-0.0130(6)
		Fraction	0.264(4)	0.259(4)	0.255(4)	0.273(4)	0.313(4)	0.325(4)	0.329(2)	0.333	0.333	0.333	0.333
		U_{iso}	0.052(2)	0.061(1)	0.061(2)	0.053(5)	0.062(4)	0.051(4)	0.061(5)	0.055(5)	0.059(5)	0.055(5)	0.062(5)
O2	**(½,0,0)**	**Fraction**	0.138(5)	0.149(5)	0.157(4)	0.121(4)	0.041(3)	0.016(2)	0.010(2)	–	–	–	–
	3*e*	U_{iso}	0.052(2)	0.061(1)	0.061(2)	0.053(5)	0.062(4)	0.051(4)	0.061(5)	–	–	–	–
O3	**(x,$\bar{x}$,z)**	***x***	0.1655(6)	0.1654(5)	0.1671(7)	0.1669(7)	0.1667(7)	0.1675(7)	0.1657(7)	0.1653(7)	0.1656(7)	0.1690(8)	0.1671(8)
	6*i*	***z***	0.1324(2)	0.1326(3)	0.1328(2)	0.1316(3)	0.1316(3)	0.1315(3)	0.1310(3)	0.1307(3)	0.1308(3)	0.1306(3)	0.1303(3)
		$U_{11} = U_{22}$	0.028(1)	0.027(1)	0.034(1)	0.041(2)	0.043(2)	0.052(3)	0.050(3)	0.055(2)	0.059(3)	0.062(3)	0.068(3)
		U_{33}	0.026(1)	0.029(2)	0.028(2)	0.035(2)	0.037(2)	0.043(2)	0.044(2)	0.044(2)	0.044(2)	0.049(2)	0.051(3)
		U_{12}	0.016(2)	0.016(2)	0.023(3)	0.028(3)	0.032(3)	0.040(3)	0.034(3)	0.041(4)	0.043(4)	0.046(4)	0.052(4)
O4	**($2\bar{x}$,$\bar{x}$,$\bar{z}$)**	***x***	0.4925(4)	0.4920(4)	0.4920(5)	0.4919(5)	0.4920(5)	0.4926(5)	0.4916(5)	0.4922(5)	0.4915(5)	0.4936(6)	0.4922(6)
	6*i*	***z***	0.2941(1)	0.2940(3)	0.2940(2)	0.2946(2)	0.2948(2)	0.2952(2)	0.2954(2)	0.2954(2)	0.2953(2)	0.2956(2)	0.2955(2)
		$U_{11} = U_{22}$	0.0119(9)	0.017(1)	0.019(1)	0.020(1)	0.023(2)	0.022(1)	0.030(2)	0.023(1)	0.030(2)	0.032(1)	0.031(2)
		U_{33}	0.015(1)	0.019(1)	0.018(2)	0.019(2)	0.017(2)	0.021(2)	0.024(2)	0.020(2)	0.025(2)	0.029(2)	0.030(2)
		U_{12}	0.0022(4)	0.0086(5)	0.0095(4)	0.0101(6)	0.0122(6)	0.0108(6)	0.0128(6)	0.0054(3)	0.0117(6)	0.0179(7)	0.0153(8)

Table S2. Continued

			50 °C	140 °C	220 °C	290 °C	350 °C	410 °C	470 °C	530 °C	590 °C	650 °C	700 °C
O5	**(*x*,$\bar{x}$,*z*)**	***x***	0.1631(4)	0.1634(4)	0.1641(6)	0.1637(6)	0.1632(6)	0.1645(7)	0.1649(6)	0.1624(7)	0.1639(7)	0.1626(7)	0.1628(7)
	6*i*	***z***	0.4319(2)	0.4322(2)	0.4322(3)	0.4317(3)	0.4320(3)	0.4320(3)	0.4316(2)	0.4319(3)	0.4323(3)	0.4324(3)	0.4322(3)
		$U_{11} = U_{22}$	0.013(1)	0.017(1)	0.018(2)	0.020(1)	0.020(2)	0.022(1)	0.023(1)	0.027(2)	0.029(2)	0.030(2)	0.031(2)
		U_{33}	0.021(2)	0.024(2)	0.020(2)	0.017(2)	0.023(2)	0.022(2)	0.021(2)	0.026(2)	0.027(2)	0.029(2)	0.030(2)
		U_{12}	0.0095(2)	0.013(1)	0.012(2)	0.013(2)	0.011(2)	0.010(1)	0.012(2)	0.016(2)	0.016(2)	0.017(2)	0.018(2)
			50 °C	**140 °C**	**220 °C**	**290 °C**	**350 °C**	**410 °C**	**470 °C**	**530 °C**	**590 °C**	**650 °C**	**700 °C**
	χ2		1.63	1.68	1.55	1.54	1.44	1.51	1.41	1.46	1.46	1.45	1.45
	Rp (%)		6.96	6.86	6.71	7.09	7.35	8.13	7.73	8.00	8.05	8.03	8.04
	Rwp (%)		7.56	7.67	7.53	7.72	7.94	8.43	8.21	8.51	8.57	8.59	8.57

The refined structural parameters are displayed in Table S2. Anisotropic displacement parameters (U_{ij}) were constrained to be the same for the Ba and Mo/Nb cations, while the ones for the oxygen atoms were freely refined. The oxygen disorder on the palmierite layers was modelled by splitting the O1 site from Wyckoff position 2*d* to 6*i* and using a single isotropic displacement parameter (U_{iso}) for O1 and O2.

As discussed in the manuscript, the O1 and O2 site cannot be simultaneously occupied, therefore partial occupancies were refined. The O3, O4, and O5 fractional occupancies refined to within ± 1% of the full occupancy and were fixed to 1. Refining the oxygen site occupancies resulted in an overall oxygen stoichiometry of O_{20}, in agreement with the nominal composition. Due to their similar neutron scattering lengths [71], the Mo and Nb cations were statistically distributed on the metal M positions. The occupancies of the Ba and M3, M4 sites refined to within ± 1% of the full occupancy and were fixed to 1. The fractional occupancies for M1 and M2 were refined. The short M1–M2 distance (~ 1.6 – 1.7 Å) indicates that simultaneous occupation of the M1 and M2 positions is highly unfavourable. Refinement of the fractional occupancies of M1 and M2 reveals that the two sites are in fact partially occupied. The M1 site is predominantly occupied. The M1 fractional occupancy increases with the temperature above 300 °C, while the M2 fractional occupancy decreases (Figure S28). A similar thermal rearrangement of the metal fractional occupancies has been reported for $Ba_3NbMoO_{8.5}$ [50, 72]. The occupancy of the M1 site is 86 – 95% of the full occupancy, revealing that the cationic vacancies are mostly distributed on the M2 site of the $Ba_7Nb_4MoO_{20}$ structure.

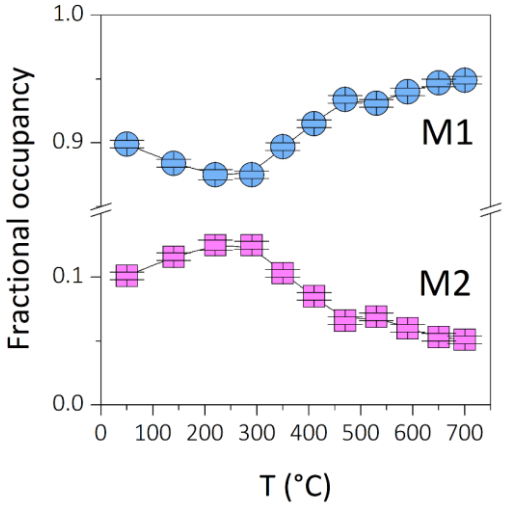

Figure S28. Variation of the M1 and M2 fractional occupancy with the temperature.

Occupation of the M2 position suggests departure from the ordered model depicted by Garcia-González *et al*, evidencing disorder of the cationic vacancies on the M1 and M2 metal sites. The cationic vacancies can be distributed on the M1 and M2 positions according to the four different possible local configurations shown in Figure 4c in the manuscript. The cationic vacancies can be arranged on the M2 sites only, thus giving the ordered palmierite - 12R perovskite stacking (configuration A in Figure 4c), or be distributed on both metal positions, forming alternated layers of occupied-unoccupied M1 and M2 sites (configurations B and C in Figure 4c). In configuration D in Figure 4c, the cationic vacancies are on the M1 sites only. Given the tendency of the M1 site to be predominantly occupied (Fig. S26) the latter configuration is however very unlikely, as it would result in under-bonded oxygen atoms.

The positional oxygen disorder on the palmierite layers and the random distribution of oxygen atoms on the O1/O2 sites produce a range of $M1O_x$ polyhedral units with variable local coordination, while the cationic disorder results in various stacking configurations accommodating the cationic vacancies. $Ba_7MoNb_4O_{20}$ clearly presents substantial local structural disorder, which underlies the average palmierite - 12R perovskite structural model. Typical bond lengths and angles are presented in Table S3. The $M1O_4$ and $M1O_6$ average polyhedral units are highly distorted, and so are the M2 and M3 octahedra; the $M4O_6$ octahedron at the centre of the 12R perovskite block is instead regular. Similar bond lengths and angles have been reported for $Ba_3NbMoO_{8.5}$ [4, 73].

Table S3. Selected atomic distances (in Å) for $Ba_7Nb_4MoO_{20}$.

	50 °C	140 °C	220 °C	290 °C	350 °C	410 °C	470 °C	530 °C	590 °C	650 °C	700 °C
M1–O1	1.793(8)	1.792(7)	1.77(2)	1.79(1)	1.83(1)	1.82(1)	1.83(1)	1.83(1)	1.83(1)	1.85(1)	1.83(1)
–O2	2.279(4)	2.270(5)	2.264(5)	2.270(5)	2.313(4)	2.310(4)	–	–	–	–	–
–O3	1.829(7)	1.839(3)	1.831(8)	1.826(8)	1.809(7)	1.804(8)	1.810(8)	1.819(8)	1.819(8)	1.787(9)	1.805(9)
M2–O3	1.998(2)	1.975(1)	1.97(2)	1.96(2)	1.98(2)	1.96(2)	1.98(3)	2.02(3)	2.00(4)	2.01(5)	2.05(5)
–O4	2.299(3)	2.32(2)	2.31(2)	2.33(2)	2.34(3)	2.37(3)	2.37(4)	2.34(4)	2.36(5)	2.33(6)	2.30(6)
M3–O4	1.871(5)	1.874(3)	1.871(6)	1.865(4)	1.867(6)	1.858(6)	1.851(6)	1.864(6)	1.857(6)	1.875(7)	1.864(6)
–O5	2.187(6)	2.184(3)	2.185(7)	2.190(7)	2.199(7)	2.205(7)	2.197(7)	2.215(7)	2.213(7)	2.226(7)	2.224(7)
M4–O5	2.003(5)	2.0053(2)	2.012(6)	2.016(6)	2.012(6)	2.025(6)	2.034(6)	2.012(6)	2.022(7)	2.011(7)	2.017(7)
M1–M2	1.71(4)	1.67(3)	1.72(3)	1.66(3)	1.64(4)	1.62(5)	1.61(6)	1.66(6)	1.63(7)	1.70(9)	1.73(9)
O1–O1	3.08(4)	3.12(4)	3.12(2)	3.11(4)	2.88(4)	2.87(4)	2.86(4)	2.87(2)	2.86(4)	2.79(3)	2.83(4)

The thermal variation of the shortest O1–O1 distance is presented in Figure S29. An abrupt decrease in the O1–O1 separation is clearly evident above 300 °C.

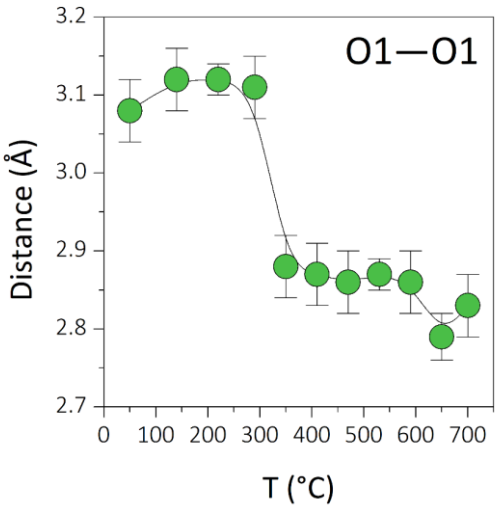

Figure S29. Temperature dependency of the shortest O1–O1 distance.

S9.2 Unit cell dimensions

The unit cell dimensions show a change in slope above 290 °C (figure S30), which is the onset temperature of the structural reorganisation.

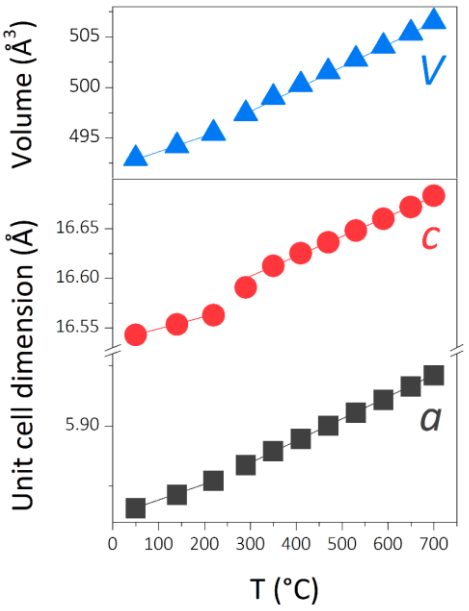

Figure S30. Thermal dependency of the unit cell parameters of $Ba_7Nb_4MoO_{20}$.

The thermal expansion coefficient (TEC) can be evaluated from the linear slopes of the unit cell parameters. The thermal expansion coefficient of the *a*-axis is 11.4 (3) x 10^{-6} $°C^{-1}$ below 290 °C, and increases to 15.4 (2) x 10^{-6} $°C^{-1}$ above 290 °C. TEC values for the *c*-axis are 7.07 (1) x 10^{-6} $°C^{-1}$ and 12.0 (3) x 10^{-6} $°C^{-1}$ below and above the transition temperature respectively. These values are close to the thermal expansion coefficient of yttria stabilised zirconia (10.8 x 10^{-6} $°C^{-1}$) and gadolinium doped ceria (12 x 10^{-6} $°C^{-1}$) [36]. The thermal expansion coefficient of $BaZr_{0.8}Y_{0.2}O_{3-\delta}$ is 10.1 x 10^{-6} $°C^{-1}$ [74].

S10. Volume change between dry and hydrated phase

The volume change between the dry and hydrated phase of $Ba_7Nb_4MoO_{20}$ was evaluated by X-ray diffraction. A dry $Ba_7Nb_4MoO_{20}$ sample was prepared by heating at 1000 °C under static air for 10 hours, while a hydrated (wet) sample was prepared by heating under humidified air flow at 900 °C for 4 hours and slowly cooling down (1 °C/min) to room temperature. Laboratory X-ray diffraction data was collected at room temperature post-annealing and accurate unit cell dimensions were determined by Rietveld analysis.

Figure S31 evidences a shift towards lower 2θ values in the reflections of the hydrated $Ba_7Nb_4MoO_{20}$ sample, indicating an expansion of the unit cell dimensions.

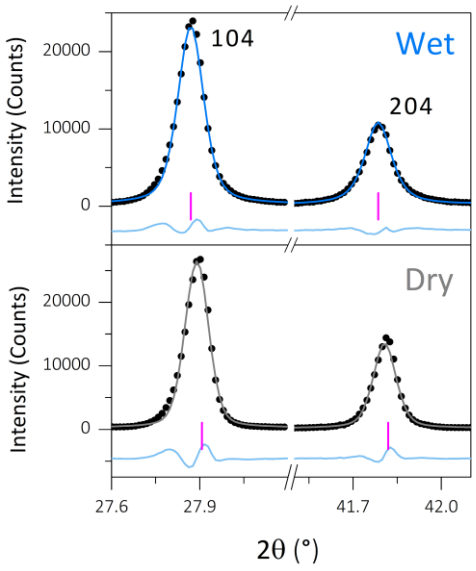

Figure S31. Rietveld fit to the X-ray diffraction data of dry and hydrated (wet) $Ba_7Nb_4MoO_{20}$. Black dots indicate the observed data, the grey and blue lines the Rietveld fit, the light blue line the difference between the observed and calculated patterns, and the pink bars the reflection positions.

The unit cell dimensions of the hydrated sample are a = 5.8837 (1) Å, c = 16.5414 (2) Å, V = 495.91 (1) Å^3, larger than the values obtained for the dry sample; a = 5.8688 (1) Å, c = 16.5258 (3) Å, V = 492.93 (1) Å^3. The volume change between the dry and hydrated phase is about 0.6%. Under similar conditions, $BaZr_{0.8}Y_{0.2}O_{3-\delta}$ shows an increase in volume of ca. 0.7% [74], while the volume of $BaSn_{0.6}Sc_{0.4}O_{3-\delta}$ shows an increase of about 1% upon deuteration [75].

References

[1] Garcia-González, E., Parras, M. & González-Calbet, J. M. Crystal structure of an unusual polytype: 7H-$Ba_7Nb_4MoO_{20}$. *Chem. Mater.* **11**, 433-437 (1999).

[2] Svensson, G. & Werner, P. E. Determination of the composition of BaO_3 using profile refinement and phase analysis. *Mat. Res. Bull*. **25**, 9-14 (1990).

[3] Wildman, E. J., Mclaughlin, A. C., Macdonald, J. F., Hanna, J. V. & Skakle, J. M. S. The crystal structure of $Ba_3Nb_2O_8$ revisited: a neutron diffraction and solid-state NMR study. *Inorg. Chem.* **56**, 2653-2661 (2017).

[4] Fop, S. *et al*. Oxide ion conductivity in the hexagonal perovskite derivative $Ba_3MoNbO_{8.5}$. *J. Am. Chem. Soc.* **138**, 16764-16769 (2016).

[5] Fop, S., Wildman, E. J., Skakle, J. M. S., Ritter, C. & Mclaughlin, A. C. Electrical and structural characterization of $Ba_3Mo_{1-x}Nb_{1+x}O_{8.5-x/2}$: the relationship between mixed coordination, polyhedral distortion and the ionic conductivity of $Ba_3MoNbO_{8.5}$. *Inorg. Chem.* **56**, 10505-10512 (2017).

[6] Ashok, A., Hausgrud, R., Norby, T., & Olsen A. Structural study of the complex perovskite $Ba_4(Ba_2Nb_2)O_{11}$. *Mat. Charact.* **102**, 71-78 (2015).

[7] Ling, C. D. *et al*. Structures, phase transitions, hydration, and ionic conductivity of $Ba_4Nb_2O_9$. *Chem. Mater.* **21**, 3853-3864 (2009).

[8] De Paoli, J. M., Alonso, J. A. & Carbonio, R. E. Synthesis and structure refinement of layered perovskites $Ba_{5-x}La_xNb_{4-x}Ti_xO_{15}$ (x=0, 1, 2, 3 and 4) solid solutions. *Journal of Physics and Chemistry of Solids* **67**, 1558-1566 (2006).

[9] Sirotinkin, S. P., Sirotinkin, V. P. & Trunov, V. K. Structure of low temperature modification of $BaNb_2O_6$. Z. Neorg. Khim. **35**, 1609-1611 (1990).

[10] Vanderah, T. A., Collins, T. R., Wong-Ng, W., Roth, R. S. & Farber, L. Phase equilibria and crystal chemistry in the BaO–Al_2O_3–Nb_2O_5 and BaO–Nb_2O_5 systems. *Journal of Alloys and Compounds* **346**, 116-128 (2002).

[11] Marinder, B. O., Dorin, E. & Seleborg, M. Studies on rutile-type phases in mixed metal dioxides. II. *Acta Chem. Scand*. **126**, 293-296 (1962).

[12] Afanasiev, P. Structure and properties of the $Mo_3Nb_2O_{14}$ oxide. *J. Phys. Chem.* **109**, 18293-18300 (2005).

[13] Lii, K. H., Wang, C. C. & Wang, S. L. Zigzag octahedral cluster chains in $BaMo_6O_{10}$. *Journal of Solid State Chemistry* **77**, 407-411 (1988).

[14] Werner, P. E., *et al*. Crystal structure of $BaMo_3O_{10}$ solved from powder diffraction data. *Z. Krist.* **212**, 665-670 (1997).

[15] Nassif, V., Carbonio, R. E. & Alonso, J. A. Neutron diffraction study of the crystal structure of $BaMoO_4$: a suitable precursor for metallic $BaMoO_3$ perovskite. *Journal of Solid State Chemistry* **146**, 266-270 (1999).

[16] Brixner, L. H. X-ray study and electrical properties of the system $Ba_{1-x}Sr_xMO_3$. *J. Inorg. Nucl. Chem.* **14**, 225-230 (1960).

[17] Turzhevsky, S. A., Novikov, D. L., Gubanov, V. A. & Freeman, A. J. Electronic structure and crystal chemistry of niobium oxide phases. *Phys. Rev. B* **50**, 3200-3208 (1994).

[18] Svensson, G., Köhler, J. & Simon, A. $BaNb_7O_9$, a new oxoniobate with double layers of corner-sharing Nb6 octahedra. *Angew. Chem. Int. Ed. Engl.* **31**, 212-213 (1992).

[19] Zubkov, V. G. *et al*. Synthesis and structural, magnetic and electrical characterisation of the reduced oxoniobates $BaNb_8O_{14}$, $EuNb_8O_{14}$, $Eu_2Nb_5O_9$ and Eu_xNbO_3 (x = 0.7, 1.0). *Journal of Alloys and Compounds* **226**, 24-30 (1995).

[20] Hessen, B., Sunshine, S. A., Siegrist, T., Fiory, A. T. & Waszczak, J. V. Structure and properties of reduced barium niobium oxide single crystals obtained from borate fluxes. *Chem. Mater.* **3**, 528-534 (1991).

[21] Svensson, G., Eriksson, L., Olofsson, C. & Holm, W. Studies on $Ba_2Nb_{5-x}Ti_xO_9$ ($0 \leq x \leq 1.75$). *Journal of Alloys and Compounds* **248**, 33-41 (1997).

[22] Wachsman, E. D. & Lee, K. T. Lowering the temperature of solid oxide fuel cells. *Science* **334**, 935-939 (2011).

[23] Jankovic, J., Wilkinson, D. P. & Hui, R. Proton conductivity and stability of $Ba_2In_2O_5$ in hydrogen containing atmospheres. *Journal of The Electrochemical Society* **158**, B61-B68 (2011).

[24] Marrero-López, D., Canales-Vázquez, J., Ruiz-Morales, J. C., Irvine, J. T. S. & Núñez, P. Electrical conductivity and redox stability of $La_2Mo_{2-x}W_xO_9$ materials. *Electrochimica Acta* **50**, 4385-4395 (2005).

[25] Goutenoire, F., Retoux, R., Suard, E. & Lacorre, P. Ab initio determination of the novel perovskite-related structure of $La_7Mo_7O_{30}$ from powder diffraction. *Journal of Solid State Chemistry* **142**, 228-235 (1999).

[26] Marrero-López, D. *et al*. Stability and transport properties of $La_2Mo_2O_9$. *Journal of Solid State Electrochemistry* **8**, 638-643 (2004).

[27] Vega-Castillo, J., Mogni, L., Corbel, G., Lacorre, P. & Caneiro, A. On the thermodynamic stability of $La_2Mo_2O_{9-\delta}$ oxide-ion conductor. *International Journal of Hydrogen Energy* **35**, 5890-5894 (2010).

[28] Fabbri, E., Pergolesi, D. & Traversa, E. Materials challenges toward proton-conducting oxide fuel cells: a critical review. *Chem. Soc. Rev.* **39**, 4355-4369 (2010).

[29] Bi, L. *et al*. Fabrication and characterization of easily sintered and stable anode-supported proton-conducting membranes. *Journal of Membrane Science* **336**, 1-6 (2009).

[30] Zakowsky, N., Williamson, S. & Irvine, J. T. S. Elaboration of CO_2 tolerance limits of $BaCe_{0.9}Y_{0.1}O_{3-\delta}$ electrolytes for fuel cells and other applications. *Solid State Ionics* **176**, 3019-3026 (2005).

[31] Yan, N. *et al*. Discovery and understanding of the ambient-condition degradation of doped barium cerate proton-conducting perovskite oxide in solid oxide fuel cells. *Journal of The Electrochemical Society* **162**, F1408-F1414 (2015).

[32] Sažinas, R., Bernuy-López, C., Einarsrud, M. & Grande, T. Effect of CO_2 exposure on the chemical stability and mechanical properties of $BaZrO_3$-ceramics. *J. Am. Ceram. Soc.* **99**, 3685-3695 (2016).

[33] Jacobson, A. J., Materials for solid oxide fuel cells. *Chem. Mater*. **22**, 660-674 (2010).

[34] Shao, Z. & Haile, S. M. A high-performance cathode for the next generation of solid-oxide fuel cells. *Nature* **431**, 170-173 (2004).

[35] Zhou, C., Sunarso, J., Song, Y., Dai, J., Zhang, J., Gu, B., Zhou, W. & Shao, Z. New reduced-temperature ceramic fuel cells with dual-ion conducting electrolyte and triple-conducting double perovskite cathode. *J. Mater. Chem. A* **7**, 13265-13274 (2019).

[36] Marrero-López, D. *et al*. Applicability of $La_2Mo_{2-y}W_yO_9$ materials as solid electrolyte for SOFCs. *Solid State Ionics* **178**, 1366-1378 (2007).

[37] Yoo, Y. & Lim, N. Performance and stability of proton conducting solid oxide fuel cells based on yttrium-doped barium cerate-zirconate thin-film electrolyte. *J. Power Sources* **229**, 48-57 (2013).

[38] Kravchyk, K. V., Quarez, E., Solís, C., Serra, J. M. & Joubert, O. Cathode materials for $La_{0.995}Ca_{0.005}NbO_4$ proton ceramic electrolyte. *Int. J. Hydrogen Energy* **36**, 13059-13066 (2011).

[39] Bernasconi, A., Tealdi, C., Mühlbauer, M. & Malavasi, L. Synthesis, crystal structure and ionic conductivity of the $Ba_3Mo_{1-x}W_xNbO_{8.5}$ solid solution. *Journal of Solid State Chemistry* **258**, 628-633 (2018).

[40] Irvine, J. T. S., Sinclair, D. C. & West, A. R. Electroceramics: characterization by impedance spectroscopy. *Adv. Mater.* **2**, 132-138 (1990).

[41] Slade, R. C. T. & Singh, N. Generation of charge carriers and an H/D isotope effect in proton-conducting doped barium cerate ceramics. *J. Mater. Chem.* **1**, 441-445 (1991)

[42] Verbraeken, M. C., Cheung, C., Suard, E. & Irvine, J. T. S. High H^- ionic conductivity in barium hydride. *Nature Materials* **14**, 95-100 (2014).

[43] Boukamp, B. A. A linear Kronig-Kramers transform test for immittance data validation. *Journal of The Electrochemical Society* **142**, 1885-1894 (1995).

[44] Boukamp, B. A. Electrochemical impedance spectroscopy in solid state ionics: recent advances. *Solid State Ionics* **169**, 65-73 (2004).

[45] Schönleber, M., Klotz, D. & Ivers-Tiffée, E. A Method for Improving the robustness of linear Kramers-Kronig validity tests. *Electrochimica Acta* **131**, 20-27 (2014).

[46] Boukamp, B. A. Practical application of the Kramers-Kronig transformation on impedance measurements in solid state electrochemistry. *Solid State Ionics* **62**, 131-141 (1993).

[47] Tao, S. & Irvine, J. T. S. Preparation and characterisation of apatite-type lanthanum silicates by a sol-gel process. *Materials Research Bulletin* **36**, 1245-1258 (2001).

[48] Kuang, X. *et al*. Interstitial oxide ion conductivity in the layered tetrahedral network melilite structure. *Nature Materials* **7**, 498-504 (2008).

[49] Kreuer, K. D., Proton-conducting oxides. *Annu. Rev. Mater. Res.* **33**, 333-359 (2003).

[50] Chambers, M. S. *et al*. Hexagonal perovskite related oxide ion conductor $Ba_3NbMoO_{8.5}$: phase transition, temperature evolution of the local structure and properties. *J. Mater. Chem. A*, **7**, 25503-25510 (2019).

[51] Zhang, G. B. & Smyth, D. M. Protonic conduction in $Ba_2In_2O_5$. *Solid State Ionics* **82**, 153-160 (1995).

[52] Norby, T., Widerøe, M., Glöckner, R. & Larring, Y. Hydrogen in oxides. *Dalton Trans.*, 3012-3018 (2004).

[53] Yang, L., Wang, S., Blinn, K., Liu, M., Cheng, Z. & Liu, M. Enhanced sulphur and coking tolerance of a mixed ion conductor for SOFCs: $BaZr_{0.1}Ce_{0.7}Y_{0.2-x}Yb_xO_{3-\delta}$. *Science* **326**, 126-129 (2009).

[54] Choi, S.et al. Exceptional power density and stability at intermediate temperatures in protonic ceramic fuel cells. *Nat. Energy* **3**, 202–210 (2018).

[55] Scherrer, B. *et al*. On Proton Conductivity in Porous and Dense Yttria Stabilized Zirconia at Low Temperature. *Adv. Funct. Mater.* **23**, 1957-1964 (2013).

[56] Ma, G., Zhang, F., Zhu, J. & Meng, G. Proton conduction in $La_{0.9}Sr_{0.1}Ga_{0.8}Mg_{0.2}O_{3-\alpha}$. *Chem. Mater.* **18**, 6006-6011 (2006).

[57] Nomura, K. & Kageyama, H. Transport properties of $Ba(Zr_{0.8}Y_{0.2})O_{3-\delta}$ perovskite. *Solid State Ionics* **178**, 661-665 (2007).

[58] Haugsrud, R. & Norby, T. Proton conduction in rare-earth ortho-niobates and ortho-tantalates. *Nature Materials* **5**, 193-196 (2006).

[59] Fop, S. Novel oxide ion conductors in the hexagonal perovskite family, PhD thesis, University of Aberdeen (2016)

[60] Jayaraman, V. *et al*. Characterization of perovskite systems derived from $Ba_2In_2O_5\square$: part II: the proton compounds $Ba_2In_{2(1-x)}Ti_{2x}O_{4+2x}(OH)_y$ [0≤x≤1; y≤2(1−x)]. *Solid State Ionics* **170**, 25-32 (2004).

[61] Omata, T., Kita, M., Goto, Y., Okura, T. & Otsuka-Yao-Matsuo, S. Formation and thermal stability of hydrate-like compounds of $Ba_2(In_{1-x}M^{III}_x)_2O_5 \cdot nH_2O$ (M^{III} = Ga, Sc, Lu, and Y). *Journal of The Electrochemical Society* **152**, A1068-A1072 (2005).

[62] Omata, T., Fuke, T. & Otsuka-Yao-Matsuo, S. Hydration behavior of $Ba_2Sc_2O_5$ with an oxygen-deficient perovskite structure. *Solid State Ionics* **177**, 2447-2451 (2006).

[63] Animitsa, I., Neiman, A., Sharafutdinov, A. & Nochrin, S. Strontium tantalates with perovskite-related structure. *Solid State Ionics* **136-137**, 265-271 (2000).

[64] Ling, C. D. *et al*. Structures, phase transitions, hydration, and ionic conductivity of $Ba_4Ta_2O_9$. *Chem. Mater.* **22**, 532-540 (2010).

[65]Norby, T. A Kröger-Vink compatible notation for defects in inherently defective sublattices. *Journal of the Korean Ceramic Society*, **47**, 19-25 (2010).

[66] Darriet, J. & Subramanian, M. A. Structural relationships between compounds based on the stacking of mixed layers related to hexagonal perovskite-type structures. *J. Mater. Chem.* **5**, 543-552 (1995).

[67] Watanabe, A. & Das, K. Time-dependent degradation due to the gradual phase change in BICUVOX and BICOVOX oxide-ion conductors at temperatures below about 500°C. *Journal of Solid State Chemistry* **163**, 224-230 (2002).

[68] Jiang, N. & Wachsman, E. D. structural stability and conductivity of phase-stabilized cubic bismuth oxides. *J. Am. Ceram. Soc.* **82**, 3057-3064 (1999).

[69] Hervoches, C. H. & Greaves, C. Crystal structure and oxide ion conductivity in cubic (disordered) and tetragonal (ordered) phases of $Bi_{25}Ln_3Re_2O_{49}$ (Ln = La, Pr). *J. Mater. Chem.* **20**, 6759-6763 (2010).

[70] Toby, B. H. EXPGUI, a graphical user interface for GSAS. *Journal of Applied Crystallography* **34**, 210-213 (2001).

[71] Sears, V. F. Neutron scattering lengths and cross sections. *Neutron News* **3**, 29-37 (1992).

[72] Fop, S. *et al*. Investigation of the relationship between the structure and conductivity of the novel oxide ionic conductor $Ba_3MoNbO_{8.5}$. *Chem. Mater.* **29**, 4146-4152 (2017).

[73] Auckett, J. E., Milton, K. L. & Evans, I. R. Cation distributions and anion disorder in $Ba_3NbMO_{8.5}$ (M = Mo, W) materials: implications for oxide ion conductivity. *Chem. Mater.* **31**, 1715-1719 (2019).

[74] Han, D., Hatada, N. & Uda, T. Chemical expansion of yttrium-doped barium zirconate and correlation with proton concentration and conductivity. *J. Am. Ceram. Soc.* **99**, 3745-3753 (2016).

[75] Kinyanjui, F. G. *et al*. Crystal structure and proton conductivity of $BaSn_{0.6}Sc_{0.4}O_{3-\delta}$: insights from neutron powder diffraction and solid-state NMR spectroscopy. *J. Mater. Chem. A* **4**, 5088-5101 (2016).